AI-assisted decoding of molecular signatures essential for NON-PHOTOTROPIC HYPOCOTYL3 condensation and function in phototropism

Prabha Manishankar,[1] Lea Reuter,[1] Leander Rohr,[1] Atiara Fernandez,[1] Yeliz Idil Yigit,[1] Tanja Schmidt,[1,2] Irina Droste-Borel,[3] Jutta Keicher,[1] Andrea Bock,[1] Claudia Oecking[1]*

[1]Center for Plant Molecular Biology (ZMBP), University of Tübingen, Tübingen, Germany.
[2]Current address: Center for Desert Agriculture, King Abdullah University of Science and Technology, Thuwal, Kingdom of Saudi Arabia
[3]Proteome Center Tübingen, University of Tübingen, Tübingen, Germany.

* Corresponding author. Email: claudia.oecking@zmbp.uni-tuebingen.de

ABSTRACT

The plasma membrane-associated protein NON-PHOTOTROPIC HYPOCOTYL 3 (NPH3) is a key component of plant phototropism. Blue light induces the release of NPH3 into the cytosol, where it dynamically transitions into membrane-less biomolecular condensates. Here, we combine experimental data with the power of AI-based protein structure prediction to uncover a bipartite C-terminal motif that enables self-interaction of NPH3. We further demonstrate its importance for both the association of NPH3 with the plasma membrane and the assembly of condensates in the cytosol, with a different part of the bipartite motif playing the key role in each case. However, the formation of cytosolic condensates additionally requires the co-operative action of an N-terminal NPH3 signature. We propose that NPH3 forms a crosslinked 3D network in the cytosol based on distinct molecular determinants that simultaneously self-associate. NPH3 variants incapable of condensation are non-functional, suggesting a fundamental role of NPH3 phase separation for phototropism. This structural snapshot could have direct implications for future analyses of the plant-specific NPH3/RPT2-Like protein family.

Introduction

The phototropic response describes the capability of plants to re-orient shoot growth towards a directional blue light (BL) source which ultimately enhances photosynthetic competence. The BL-activated and plasma membrane (PM)-associated AGCVIII kinases, phototropin1 (phot1) and phot2, function as primary photoreceptors. Asymmetric growth of the hypocotyl is based on the establishment of a lateral auxin gradient with a higher hormone concentration on the shaded side (Christie & Murphy, 2013; Fankhauser & Christie, 2015; Haga & Sakai, 2023; Küpers *et al*, 2020; Legris & Boccaccini, 2020). Accordingly, certain members of the PIN-FORMED (PIN) family of auxin efflux carriers are required for phototropic hypocotyl bending (Willige *et al*, 2013). In addition to the regulation of PIN activity by a family of AGCVIII protein kinases (D6 PROTEIN KINASES) (Willige *et al*, 2013; Zourelidou *et al*, 2014), alterations in the subcellular polarity of PIN proteins, particularly PIN3 (Ding *et al*, 2011; Zhang *et al*, 2017), are known to mediate the effect of BL on auxin distribution (Fankhauser & Christie, 2015; Hohm *et al*, 2013; Legris & Boccaccini, 2020). Although the mechanism linking photoreceptor activation to PIN protein modulation is still unknown, recent data have revealed that dynamic changes in the subcellular localization of the early phototropic signaling component NON-PHOTOTROPIC HYPOCOTYL 3 (NPH3) are crucial for phot1 signaling (Reuter *et al*, 2021; Sullivan *et al*, 2021). In darkness, NPH3 associates to the PM (Haga *et al*, 2015; Sullivan *et al*, 2019) in a phospholipid-dependent manner (Reuter *et al*, 2021) and physically interacts with the photoreceptor phot1 (Motchoulski & Liscum, 1999 ; Haga *et al*, 2015). Following BL perception, phot1 directly phosphorylates the third last residue (S744) of NPH3 (Sullivan *et al*, 2021), which represents a C-terminal 14-3-3 binding motif. Subsequent association of 14-3-3 proteins is causal for the light-induced release of NPH3 from the PM into the cytosol. This BL-induced relocation of NPH3 precedes its dynamic transitions into membrane-less condensate-like particles in the cytosol (Reuter *et al*, 2021; Sullivan *et al*, 2021). Importantly, the light-induced processes are reversible, eventually resulting in PM re-association of NPH3 (Haga *et al*, 2015; Reuter *et al*, 2021). Moreover, NPH3 mutants constitutively localizing to either the PM (incapable of 14-3-3 binding, e.g. NPH3_S744A) or condensates (impaired in PM association, e.g. NPH3ΔC51, NPH3_4K/A) show compromised functionality, consistent with a model where phototropic curvature critically depends on the 14-3-3 mediated dynamic change in NPH3 localization, ultimately leading to a gradient of NPH3 subcellular localization across the hypocotyl (Reuter *et al*, 2021; Sullivan *et al*, 2021).

Together with ROOT PHOTOTROPISM 2 (RPT2), NPH3 is the founding member of the plant-specific NPH3/RPT2-Like (NRL) protein family consisting of 33 members in

Arabidopsis (Christie *et al*, 2018; Pedmale *et al*, 2010). Several of them act – comparable to NPH3 – as signal transducers in processes involving auxin (re)distribution in response to developmental or environmental cues, most likely via regulation of PIN auxin carriers (Cheng *et al*, 2007; Furutani *et al*, 2007; Li *et al*, 2011; Treml *et al*, 2005). Indeed, MAB4/ENP-Like (MEL) polypeptides were recently shown to maintain PIN polarity by limiting lateral diffusion (Glanc *et al*, 2021). Considering that several NRL proteins are potential direct substrate targets of the phot AGCVIII kinases (Sullivan *et al*, 2021; Waksman *et al*, 2023) and can interact with 14-3-3 via the corresponding phosphorylated motif (Reuter *et al*, 2021), phosphorylation-dependent 14-3-3 association may represent a more general regulatory mechanism. Noteworthy, MEL proteins also form particle-like structures in the cytosol (Furutani *et al*, 2007; Furutani *et al*, 2011; Glanc *et al*, 2021) that are reminiscent of NPH3 condensates, in addition to localization at the PM.

Membrane-less biomolecular condensates emerge as a fundamental mechanism to compartmentalize cellular functions. In plants, condensate assembly appears to link environmental cues to development (Emenecker *et al*, 2021; Field *et al*, 2023) and, as usual, is driven by multivalent macromolecular interactions (Banani *et al*, 2017; Lyon *et al*, 2021; Shin & Brangwynne, 2017). NRL family members are mostly characterized by a central NPH3 domain and two putative protein interaction domains, namely an N-terminal bric-a-brac, tramtrack and broad complex (BTB) domain and a C-terminal coiled-coil (CC) domain (Christie *et al*, 2018). To date, our understanding of the structure-function relationship is very limited, making it impossible to address the question of whether condensate formation of PM-detached NPH3 is essential for its action. Accurately modeling the structures of proteins and their complexes using artificial intelligence (AI) is revolutionizing molecular biology (Evans *et al*, 2022; Jumper *et al*, 2021). Here, we closely link experimental data and AI-based protein structure predictions to decipher the molecular functions of the structured NPH3 domains. We report the identification of a bipartite C-terminal self-association motif that enables formation of homo-oligomers, likely trimers, and is required for both PM association of NPH3 in darkness and BL-triggered condensate assembly in the cytosol. The bipartite motif consists of the CC domain and a yet undescribed Linear Interacting Peptide (LIP) at the C-terminal end of the NPH3 domain. Remarkably, only the LIP-mediated self-association of NPH3 with low affinity is essential for the transition to the condensed state. In addition, the N-terminal BTB domain contributes directly to the oligomeric states of NPH3 in cytoplasmic assemblies. Overall, we propose the conversion of a strict C-terminal self-association of NPH3 at the PM into a higher-order 3D self-crosslinking in the cytosol mediated by co-operative self-association of both the LIP motif and the BTB domain. Several NPH3 variants incapable of condensate formation are non-functional, suggesting that the temporal regulation of the BL-induced NPH3 cycling between the PM and the cytosol is critical for its function in auxin-dependent phototropism.

Results

NPH3 self-associates independently of its subcellular localization and its BTB domain

According to protein signature models NPH3 possesses an N-terminal BTB, a central NPH3 and a C-terminal CC domain (Christie *et al*, 2018). Structure prediction by AI-based tools AlphaFold2 (AF2) (Jumper *et al*, 2021) or AF3 (Abramson *et al*, 2024), confirmed the above domains, each characterized by defined secondary structures and high confidence scores (per residue predicted Local Distance Difference Test, pLDDT). In addition, six intrinsically disordered regions (IDR), showing low pLDDT values and covering about 40% of the protein, are distributed along the entire length of NPH3 (Figs. 1A and EV1A). Nevertheless, the positions (Predicted Aligned Error, PAE) of the structured domains are well-defined relative to each other – with the exception of the CC domain (Fig. EV1B).

113 Protein condensate formation relies on multivalent interactions. Since NPH3 variants that
114 constitutively form cytosolic condensates (NPH3ΔC51, NPH3_4K/A) strictly co-localize
115 when transiently co-expressed in *N. benthamiana* leaves (Reuter *et al*, 2021) (Fig. 1B), we
116 wondered whether NPH3 associates with itself in cytoplasmic assemblies. Stringent co-
117 immunoprecipitation (CoIP) of fluorophore-tagged proteins confirmed their physical
118 association (Fig. 1C). However, NPH3 self-association is not restricted to cytosolic
119 assemblies but also occurs at the PM (NPH3/NPH3 darkness) (Fig. 1 B,C). Remarkably,
120 condensate-localizing RFP:NPH3ΔC51 uniformly associated with the PM in the dark when
121 co-expressed with GFP:NPH3 (Fig. 1B), implying that self-association of NPH3 enables the
122 relocation of cytosolic variants to the PM. This phenomenon is hereafter referred to as self-
123 association linked to relocation. Subsequent BL irradiation triggered co-localization of
124 RFP:NPH3ΔC51 and GFP:NPH3 in cytosolic assemblies (Fig. 1B). Conversely, PM retention
125 in BL was observed when RFP:NPH3ΔC51 or RFP:NPH3 were co-expressed with the
126 constitutively PM-localized GFP:NPH3_S744A mutant (Reuter *et al*, 2021; Sullivan *et al*,
127 2021) (Fig. EV1C). In each case, association of NPH3 variants was validated by CoIP (Figs.
128 1C and EV1D). The BTB domain has often been associated with homo- or hetero-
129 multimerization of NRL family members (Christie & Murphy, 2013; Inada *et al*, 2004;
130 Pedmale *et al*, 2010; Upadhyay-Tiwari *et al*, 2024). However, deletion of the BTB domain
131 (NPH3ΔN197) had no effect on self-association at the PM or the ability to translocate
132 RFP:NPH3ΔC51 to the PM in darkness (Figs. 1B,C and EV1C). Consequently, BTB-
133 independent self-association of NPH3 at the PM (dark) might be coupled with the dynamic
134 formation of higher-order homo- or hetero-oligomers in the cytosol (BL), ultimately leading
135 to condensate formation.
136
137 **AlphaFold2-multimer assisted identification of a bipartite C-terminal self-association**
138 **motif**
139 We next examined whether the CC domain of NPH3 contributes directly to self-association
140 linked to relocation. When NPH3 lacking the CC domain (NPH3ΔC104) was co-expressed
141 with NPH3 in darkness, it formed condensate-like particles near the PM (Fig. 2A) – an
142 obvious difference to the uniform PM localization of NPH3ΔC51 (Fig. 1B). In BL, however,
143 NPH3ΔC104 behaves like NPH3ΔC51, as it co-localizes with NPH3 in cytosolic condensates.
144 Co-localization in condensates was also observed when NPH3ΔC104 was co-expressed with
145 NPH3ΔC51 or itself (Figs. 2A and EV2A). Semi-quantitative CoIP revealed that
146 NPH3ΔC104 – when compared to NPH3ΔC51 - associated significantly weaker with NPH3,
147 NPH3ΔC51 or itself, although complex formation was still detectable (Figs. 2B and EV2B).
148 We thus hypothesized that the CC domain promotes a high-affinity interaction essential for
149 self-association linked to relocation. By contrast, the remaining weak interaction capability of
150 NPH3ΔC104 might be sufficient to contribute to multivalency-driven condensate assembly.
151 To unveil potential homomeric NPH3 interfaces, AF2-Multimer (AF2M), a protein complex
152 structure prediction tool (Evans *et al*, 2022), and AF3 (Abramson *et al*, 2024) were used.
153 Given the experimental evidence for the importance of the CC (Fig. 2B and EV2B), particular
154 attention was paid to the confidence score for this domain. On this basis, NPH3 will most
155 likely form a trimer (Fig. EV2C), which serves as a lead structure for a homooligomer (≥3) in
156 the following. Confidence scores (pLDDT) of the AF3 prediction were lower than those of
157 AF2M – probably due to the multitude of IDRs in NPH3 (see https://alphafoldserver.com,
158 limitations of the AF3 model). As the models do not differ in principle, the AF2M predictions
159 are shown below. Trimer formation of NPH3 is facilitated by small interfaces, particularly the
160 CC super helices (Figs. 2C and EV3A), which are likely to be located near the PM, as the
161 amphipathic helix required for PM association (arrows Fig. 2C) is found in the adjacent
162 region (Reuter *et al*, 2021). Excitingly, upstream of the CC trimer, AF2M predicts another
163 three-helical bundle. Here, a Linear Interacting Peptide (LIP) (MobiDB: $_{592}$LRV**VVQVLF**,

164 highlighted in yellow in all ribbon plots and schemes of NPH3) might establish hydrophobic
165 helix-helix interfaces. The so far unrecognized LIP represents the (almost) C-terminal end of
166 the NPH3 domain, exhibiting high sequence identity within the NRL family (Motchoulski &
167 Liscum, 1999) (Fig. EV3B). In each trimeric NPH3 subunit, the entire region encompassing
168 the BTB and NPH3 domains, including LIP, adopts a conformation close to that of the NPH3
169 monomer, while the position of the CC appears to be flexible in relation to the rest of the
170 protein (PAE plot, Fig. EV3A). Due to the putative LIP interactions, the NPH3 trimer exhibits
171 an almost perfect rectangular arrangement of its monomeric subunits. A view from below
172 shows a symmetrically arranged 3-bladed propeller with the LIP-trimer in its center (Fig. 2C
173 bottom).
174 We first validated CC-mediated homo-oligomerization of NPH3 by size exclusion
175 chromatography of recombinant C-terminal NPH3 fragments tagged with $(His)_6$-maltose-
176 binding protein (MBP). While the MBP:NPH3-C51 (C-terminal 51 residues) fusion protein
177 (MW: 48.2 kDa) eluted at a volume indicative of a monomer (15 ml, approx. 47 kDa), the
178 presence of the CC domain (MBP:NPH3-C104, C-terminal 104 residues, MW: 54.4 kDa)
179 resulted in a significant shift in the elution peak, suggesting a native molecular weight
180 consistent with a trimer (12 ml, approx. 166 kDa), with a small fraction detectable as a
181 hexamer (10.5 ml, approx. 346 kDa) (Fig. EV3C). To destabilize the CC superstructure, three
182 hydrophobic residues (Fig. 2D: W650, L664, M681) were replaced with glutamic acid
183 (NPH3_WLM/E). Indeed, MBP:NPH3-C104_WLM/E significantly impaired homo-
184 oligomerization of the CC, likely resulting in a monomeric state (14 ml, approx. 74 kDa) (Fig.
185 EV3C).
186 Based on this, we tested our hypothesis of CC-mediated high-affinity self-association of
187 NPH3 linked to relocation. In contrast to GFP:NPH3, GFP:NPH3_WLM/E was unable to
188 uniformly relocate RFP:NPH3ΔC51 to the PM in darkness (Fig. 2D), and its ability to bind
189 NPH3ΔC51 was markedly reduced (Fig. 2B). However, upon BL treatment,
190 GFP:NPH3_WLM/E and NPH3ΔC51 exhibited co-localization in cytoplasmic assemblies
191 (Fig. 2D). Overall, this reflects the concurrent expression of PM-associated NPH3 and
192 cytosolic NPH3ΔC104, which lacks the CC domain (Fig. 2A). We therefore concluded that
193 the CC domain is essential for the high-affinity self-association of NPH3 linked to relocation.
194 According to the structural prediction, the LIP motif may represent the molecular signature
195 allowing for weak interaction and potentially condensate formation of NPH3 variants
196 impaired in CC-mediated high-affinity interaction (NPH3ΔC104, NPH3_WLM/E). Notably,
197 AF2M still predicts the formation of a trimer for NPH3ΔC104, with high confidence scores
198 for LIP residues at the trimer interface (Fig. EV3D). By contrast, trimer formation is not
199 supported by AF2M if the LIP motif is additionally truncated (NPH3ΔC164). Co-expression
200 analyses demonstrated a preferential cytosolic localization of NPH3ΔC164 and a clear
201 separation from the strictly condensate-forming NPH3ΔC51 as well as from NPH3 both in
202 darkness and upon BL irradiation (Figs. 2A and EV2A). Moreover, semi-quantitative CoIP
203 analyses revealed a clear stepwise decrease in avidity: compared to NPH3ΔC51, deletion of
204 the CC (NPH3ΔC104) led to a significantly reduced but still detectable association, while
205 additional truncation of the LIP motif (NPH3ΔC164) almost abolished complex formation
206 with NPH3 or NPH3ΔC51. A comparable gradual decrease in interaction was also observed
207 for the co-expression of the respective C-terminally deleted NPH3 variants (Figs. 2B and
208 EV2A,B).
209 To substantiate the involvement of the LIP motif in self-association of NPH3, *in planta*
210 Förster resonance energy transfer (FRET) by fluorescence lifetime imaging (FLIM) was
211 performed. Given the mobility of condensates, constitutively PM-associated
212 GFP:NPH3_S744A was used as donor, while RFP-tagged NPH3 variants served as acceptors.
213 The percentage of interaction pixels (IPS), defined by strongly reduced fluorescence lifetime
214 (FLT) of GFP (Bücherl *et al*, 2013), was quantified. A notable increase in IPS was observed

215 when RFP-tagged NPH3 was co-expressed with the donor (32% IPS, compared to 13% IPS of
216 donor-only). Destabilization of the CC-superstructure resulted in a reduced IPS proportion
217 (RFP:NPH3_WLM/E, 21% IPS), although this was still significantly higher than the donor-
218 only control. In contrast, no substantial difference in IPS was detected when, in addition to
219 CC destabilization, self-association of the LIP motif was impaired
220 (RFP:NPH3ΔLIP_WLM/E, 15% IPS) (Fig. 2E). In this mutant variant, deletion of the 9 aa
221 LIP motif ($_{592}$LRV**VVQVLF**) served to prevent low-affinity homo-oligomerization.
222 Taken together, these results suggest a bipartite C-terminal self-association motif in NPH3
223 (Fig. 2F), consisting of the CC domain, which mediates high-affinity homo-oligomerization
224 required for relocation, and the LIP motif, which facilitates a low-affinity interaction that
225 appears sufficient for transitioning NPH3 into a condensed state in the cytosol.
226
227 **The bipartite C-terminal self-association motif is required for plasma membrane**
228 **recruitment of NPH3 in darkness**
229 The region downstream of the CC, NPH3-C51, contains the amphipathic helix crucial for
230 phospholipid-dependent PM association (Figs. 1A and 2C arrows). Despite its direct binding
231 to phospholipids *in vitro* (Reuter *et al*, 2021), RFP:NPH3-C51 surprisingly failed to associate
232 with the PM *in vivo* (Fig. 3A,B). However, extension by the CC domain (RFP:NPH3-C104)
233 enabled PM association in darkness, as confirmed by subcellular fractionation (Fig. 3B,C).
234 Membrane targeting of RFP:NPH3-C104 was in turn impaired when formation of CC
235 homooligomers (RFP:NPH3- C104_WLM/E) or alternatively phospholipid binding of NPH3
236 (RFP:NPH3-C104_4K/A, see (Reuter *et al*, 2021)) was reduced (Fig. 3B,C). Overall, PM
237 recruitment of NPH3-C104 in darkness requires both homo-oligomerization and phospholipid
238 interaction.
239 Analysis of full-length NPH3 variants aimed to understand the role of the LIP motif in PM
240 attachment. Deletion of the 9 aa comprising LIP motif ($_{592}$LRV**VVQVLF**) served as a means
241 to prevent the LIP-mediated low-affinity homo-oligomerization (RFP:NPH3ΔLIP) and had no
242 apparent effect on PM association (Fig. 3D,E). Disruption of the homotypic CC interaction
243 shifted a proportion of RFP:NPH3_WLM/E to the soluble fraction following subcellular
244 fractionation, but the shift was substantially smaller compared to NPH3-C104_WLM/E,
245 which lacks the LIP motif (Fig. 3C,E). Remarkably, the full-length RFP:NPH3_WLM/E
246 clearly localized to the cell periphery, suggesting weak PM attachment *in vivo,* likely due to
247 LIP-mediated low-affinity self-association. In fact, a significant impairment of PM
248 recruitment was only observed when the self-association of both parts of the bipartite
249 structured motif was disturbed (RFP:NPH3ΔLIP_WLM/E) (Fig. 3D,E).
250 We therefore concluded that the bipartite C-terminal self-association motif acts unequally
251 redundant for NPH3 membrane recruitment, with the CC domain fully compensating for loss
252 of the LIP motif. However, when CC homo-oligomerization is impaired, the LIP motif
253 partially compensates and facilitates weak PM association of NPH3, probably due to low-
254 affinity self-association.
255
256 **Molecular NPH3 signatures essential for condensate formation**
257 Biomolecular condensates typically form via liquid-liquid phase separation, and their
258 formation relies on multivalent molecules. Multivalency in proteins can be achieved by
259 structured interaction domains, IDRs or a combination of both (Banani *et al*, 2017).
260 We have recently reported that BL irradiation initially triggers re-localization of NPH3 from
261 the PM to the cytosol, where it dynamically transitions to a condensed state. While 14-3-3
262 association is critical for initial PM detachment of NPH3, it is not required for condensate
263 assembly as shown by the analysis of various NPH3 mutant proteins, including full-length
264 variants (Reuter *et al*, 2021). Phase separation may therefore be due to intrinsic properties of
265 NPH3 when a critical concentration in the cytosol is exceeded.

Our co-expression data suggested that deletion of the C-terminal bipartite motif prevents condensate formation (NPH3ΔC164) (Fig. 2A). Single expression of NPH3ΔC164 confirmed the direct contribution of the bipartite motif to the oligomeric states of NPH3 in cytoplasmic assemblies (Figs. 4A,B). However, exclusive interference with CC formation (NPH3ΔC104, NPH3_WLM/E) only marginally affected condensate assembly of NPH3, and, unexpectedly, deletion of the LIP motif alone (NPH3ΔLIP) abolished transition of cytosolic NPH3 to the condensed state (Fig. 4A,B). Replacement of four hydrophobic/uncharged residues potentially involved in hydrophobic LIP-LIP interfaces with alanine or glutamic acid ($_{592}$LRV**V**V**QV**L**F**SEQ ⇒ $_{592}$ERV**V**A**QV**E**F**SEA) (NPH3_4LVQ/EA, Fig. EV4A) revealed that lack of homotypic LIP interactions is causal for the loss of phase separation ability of NPH3ΔLIP (Fig. 4A). Taken together, the CC domain and the LIP motif act non-redundantly in condensate formation of NPH3: here, the LIP motif is instrumental, while the CC is dispensable.

Multivalency describes the ability to participate in more than one interaction. Deletion of the BTB domain (GFP:NPH3ΔN197) has no effect on high-affinity self-association of NPH3 at the PM (Fig. 1B,C) but prevents BL-triggered phase separation in the cytosol (Figs. 4A,B), indicating that it represents another essential NPH3 interaction valence. Collectively, BTB-independent self-association of NPH3 at the PM (dark) appears to be linked to the dynamic formation of BTB-dependent higher-order homo- or hetero-oligomers in the cytosol (BL).

The BTB domain of NRL protein family members is characterized by a conserved alpha-helical extension at the C-terminus (α6-α8, highlighted in light blue in all ribbon plots and schemes of NPH3) of the core BTB fold (β-sheets B1-B3, α-helices A1-A5) (Bonchuk *et al*, 2023). BTB domains enable protein-protein interactions, including multimerization and interactions with non-BTB proteins (Stogios *et al*, 2005). Potential interaction partners of GFP:NPH3 were identified in etiolated seedlings maintained in darkness or irradiated with BL (1 µmol $m^{-2}s^{-1}$, 30 min) by IP experiments coupled with mass-spectrometry (MS) based protein identification. With the exception of 14-3-3 proteins, no polypeptides enriched in cytosolic condensates (i.e. following BL) and showing a relative abundance of ≥1% of the bait protein could be identified (Table EV1), confirming previous results (Sullivan *et al*, 2021). Considering that 14-3-3 binding is not required for condensate formation of NPH3 (Reuter *et al*, 2021), we hypothesized that NPH3 forms a single-component condensate that may contain associated proteins such as 14-3-3. This in turn implies that the BTB domain can also establish homotypic interactions. According to AF2M, NPH3ΔC164 (devoid of the bipartite motif) could form dimers via its BTB domain (Fig. EV4B). NPH3 could therefore be a single hub that can simultaneously homopolymerize via two distinct structural domains in its N- and C-terminus, respectively. Given the reversibility of condensate formation (Haga *et al*, 2015; Reuter *et al*, 2021), the putative BTB-BTB interaction is most likely weak and occurs spontaneously. 1,6 Hexanediol disrupts weak hydrophobic interactions and has often been used to dissolve condensates (Mosesso *et al*, 2024; Dolde *et al*, 2023). The number of GFP:NPH3ΔC51 condensates decreased significantly upon 1,6 hexanediol treatment *in vivo* (Fig. 4C), suggesting that weak hydrophobic interactions indeed play a key role in phase separation of NPH3. In this context, it is of particular importance that the BTB domains apparently dimerize antiparallel, so that the second BTB domain is rotated by approx. 110°. Consequently, crosslinking of individual NPH3 trimers via BTB-mediated antiparallel interactions could enable the formation of network-like 3D assemblies, characterized by rotated positions of the individual trimers (Figs. 4D and EV4B,C). The hypothetical antiparallel BTB-BTB interaction relies on hydrophobic interactions between helices A5 of the core BTB and α8 of the C-terminal extension (Fig. EV4B). Deletion of the C-terminal extension (NPH3ΔBTBα6-8) or helix α8 alone (NPH3ΔBTBα8) prevented NPH3 condensation (Fig. 4E). The C-terminal extension of the plant-specific BTB domain is thus crucial for polymerization of NPH3 in the cytosol. However, we cannot exclude that non-

317 BTB proteins or BTB proteins different from NPH3 are involved in and required for the
318 formation of cytoplasmic NPH3 assemblies.
319 Finally, why does disruption of the hydrophobic LIP-LIP interfaces
320 (NPH3ΔLIP/NPH3_4LVQ/EA) abolish phase transition of NPH3, despite the presence of the
321 BTB domain and self-interacting CC domain? According to AF2M, deletion of the LIP motif
322 causes a breakdown of the symmetric right-angle conformation of the individual NPH3
323 monomers within the trimer/homooligomer. As a result, the BTB domains are in close contact
324 to each other, with helices A5 and α8 of the individual monomers facing each other (Fig.
325 EV4D). We therefore assume that the formation of antiparallel BTB-BTB interactions is
326 almost impossible.
327
328 **Phot1-dependent dephosphorylation of NPH3 does neither require condensate**
329 **formation nor PM dissociation**
330 Based on our novel data, we addressed open questions regarding the complex changes in
331 phosphorylation patterns of NPH3. In dark-grown seedlings, multiple residues in the
332 N-terminal IDRs of the PM-associated NPH3 are phosphorylated independently of the
333 photoreceptor phot1 (Kimura *et al*, 2021; Pedmale & Liscum, 2007; Tsuchida-Mayama *et al*,
334 2008). BL induces an immediate phosphorylation of the third-last residue of NPH3 (S744),
335 triggering association with 14-3-3, followed by PM release of NPH3 and dephosphorylation
336 of the N-terminal residues (Reuter *et al*, 2021; Sullivan *et al*, 2021). This light-induced and
337 phot1-dependent dephosphorylation of NPH3 is visualized by a slight shift in electrophoretic
338 mobility of NPH3 (Haga *et al*, 2015; Kimura *et al*, 2021; Pedmale & Liscum, 2007; Tsuchida-
339 Mayama *et al*, 2008).
340 It is not known whether phot1-dependent dephosphorylation (N-terminal IDRs) requires PM
341 dissociation and/or phase transition of NPH3 in the cytosol. Despite the inability of
342 NPH3ΔN197, GFP:NPH3ΔBTBα8 and NPH3ΔLIP to form condensates, BL irradiation
343 induces (i) phosphorylation of their third last residue (Fig. 5A) and (ii) PM-detachment (Fig.
344 EV5). Additionally, (iii) a shift in electrophoretic mobility is evident, demonstrating their
345 phot1-dependent dephosphorylation. Furthermore, all light-induced processes revert upon re-
346 transfer to darkness (Fig. 5A), eventually leading to PM re-association of the condensate-
347 incompetent variants (Fig. EV5). Overall, we concluded that (i) the analyzed NPH3 variants
348 exhibit the typical properties of native NPH3, except for phase separation in the cytosol, and
349 (ii) condensation is not required for the dephosphorylation of NPH3 observed upon phot1
350 activation.
351 However, the condensate-localizing NPH3_4K/A mutant is constitutively dephosphorylated
352 in transgenic Arabidopsis seedlings (Reuter *et al*, 2021) as well as in transiently expressing *N.*
353 *benthamiana* leaves (Fig. 5B). This suggests that either phot1-dependent dephosphorylation is
354 linked to cytosolic localization of NPH3 or phot1-independent phosphorylation of NPH3-
355 IDRs requires PM localization. We therefore relocated NPH3_4K/A to the PM in the dark by
356 simultaneous expression with NPH3 (Fig. 5C). PM association resulted in a substantial
357 portion of NPH3_4K/A exhibiting reduced electrophoretic mobility indicative of
358 phosphorylation (Fig. 5B). It is worth mentioning that BL irradiation triggers
359 dephosphorylation of NPH3_4K/A, not only when co-expressed with NPH3, but also with
360 NPH3_S744A which keeps NPH3_4K/A attached to the PM (Fig. 5B,C). In summary, PM
361 dissociation is dispensable for phot1-dependent dephosphorylation, whereas phot1-
362 independent phosphorylation in the dark (N-terminal IDRs) requires PM association of NPH3.
363 The electrophoretic mobility shift observed for the condensation-deficient NPH3 variants
364 after re-transfer to darkness (Fig. 5A) therefore confirms their re-association with the PM.
365
366 **Condensate formation of NPH3 might be key to function**

367 Recent studies have emphasized the critical role of light-triggered NPH3 cycling between the
368 PM and the cytosol in phototropism (Reuter *et al,* 2021; Sullivan *et al,* 2021). However, the
369 functional relevance of NPH3 phase separation in the cytosol remains unclear. As previously
370 described, GFP:NPH3 was fully functional in restoring the severe impairment of hypocotyl
371 phototropism in *nph3-7*, regardless of whether expression was driven by its native or the 35S
372 promoter (Haga *et al*, 2015; Reuter *et al*, 2021; Sullivan *et al*, 2019; Sullivan *et al*, 2021). By
373 contrast, ectopic expression of condensation-deficient NPH3 variants failed to complement
374 the phenotype (Figs. 6A and EV6), suggesting that NPH3 phase separation is of importance
375 for NPH3 function. However, GFP:NPH3ΔBTBα6-8 lacks the C-terminal extension of the
376 BTB domain, and deletion of the LIP motif (NPH3ΔLIP) could indirectly affect BTB-
377 dependent interactions through conformational rearrangement (Fig. EV4D). The limited
378 function of these variants might thus alternatively be caused by loss of an essential BTB-
379 dependent NPH3 interaction partner. A prime candidate in this regard is RPT2, which is
380 required for hypocotyl phototropism (Haga *et al*, 2015) and has been reported to interact with
381 NPH3 via the BTB domain. Here, the N-terminal domains of the respective proteins were
382 tested in a yeast two hybrid assay (Inada *et al*, 2004). However, through stringent CoIP we
383 found that the deletion of the BTB domain of NPH3 does not affect the physical association
384 between fluorophore-tagged NPH3 and RPT2 (Fig. 6B). We therefore concluded that RPT2
385 associates with NPH3 *in planta* independent of its BTB domain. Considering that the typical
386 features of NPH3, such as phosphorylation status and changes in subcellular localization, are
387 preserved in phase transition-deficient NPH3 variants (Figs. 5A, EV5 and 6C), the most likely
388 explanation for the impaired function is the inability to form condensates. We assume that
389 condensation serves to sequester NPH3 in the cytosol to delay re-cycling back to the PM.
390 Considering the reversibility of this process, the balanced temporal regulation of NPH3
391 cycling between the PM and the cytosol seems to be central to phototropic hypocotyl bending.
392
393 **Discussion**
394 Our data provide novel insights into molecular signatures of NPH3 defining its function in
395 BL-induced phototropic hypocotyl bending. We applied a combination of live-cell imaging,
396 deep learning-based structure prediction, biochemical, genetic and physiological approaches
397 to uncover unique, overlapping and cooperative roles of NPH3 motifs essential for self-
398 association at the PM and/or the formation of multivalency-driven condensates in the cytosol.
399 Members of the plant NRL protein family are mostly characterized by three domains, the N-
400 terminal BTB-, the central NPH3 domain and the C-terminal CC domain, all of which are
401 known since decades (Motchoulski & Liscum, 1999). However, our understanding of the
402 structure-function relationships of NRL's is quite limited.
403 *In vivo* protein-protein interaction assays, combined with confocal imaging of *N. benthamiana*
404 leaf epidermis cells expressing NPH3 variants revealed a crucial role of the CC domain in
405 mediating high-affinity self-association of NPH3 at the PM (Fig. 2A,B). Although
406 deletion/destabilization of the CC (NPH3ΔC104/NPH3_WLM/E) substantially impaired the
407 interaction strength, weak homo-oligomerization and, above all, condensate formation could
408 still be observed (Figs. 2A,B,E and 4A). AF2M/AF3 predicted the formation of NPH3
409 homooligomers (≥3), most likely trimers and provided previously unexpected molecular
410 insights that eventually led to the discovery of a bipartite C-terminal self-association motif. In
411 fact, the trimeric NPH3 complex appears to be stabilized by (i) the CC superhelices and (ii) a
412 helical bundle formed by a yet unrecognized upstream structural feature, the LIP motif (Fig.
413 2C). Experimental validation confirmed homo-oligomerization of the CC domain (Fig.
414 EV3C) and emphasized the role of the LIP motif in establishing low-affinity homomeric
415 association (Figs. 2B,E and EV2B). The LIP motif localizes to the C-terminal end of the
416 NPH3 domain and has received little attention to date. However, considering that about one
417 third of the 33 members of the NRL protein family are devoid of a CC domain (Pedmale *et al*,

418 2010), while the LIP motif is highly conserved (Fig. EV3B), LIP-mediated self-association
419 with low affinity is most likely a functionally significant feature. This is supported by the –
420 exclusively LIP-mediated - trimer formation of NPH3ΔC104 predicted by AF2M (Fig.
421 EV3D).
422 Since NPH3 homo-oligomerization is mediated by a bipartite structured motif, we examined
423 whether its individual parts serve distinct functions. Self-association linked to relocation
424 appears to be a unique feature of the CC domain and could potentially alter the subcellular
425 localization of cytosolic NRLs through heteromeric complex formation with a PM-associated
426 member. The second molecular function of the bipartite motif relates to PM association of
427 NPH3. Here, we demonstrated that homo-oligomerization of NPH3 in addition to its
428 electrostatic interaction with phospholipids (Reuter *et al*, 2021) is essential for PM
429 recruitment (Fig. 3B-D). A comparable scenario has been described for nanodomain-
430 organizing REMORINs (Martinez *et al*, 2019). Homo-oligomerization of NPH3 could enable
431 folding/exposure of the amphipathic helix, which is essential for phospholipid binding, or
432 alternatively increase avidity towards phospholipids. In the context of PM attachment, the two
433 parts obviously have an unequally redundant function. While the CC domain mediates strong
434 PM association, the LIP motif facilitates weak PM binding when the CC domain is
435 destabilized (NPH3_WLM/E) (Fig. 3 D,E). Thirdly, the C-terminal bipartite self-association
436 motif contributes to the higher-order oligomeric states of phase-separated NPH3
437 (NPH3ΔC164) (Fig. 4A). Notably, only the LIP motif (low affinity) is of importance here and
438 acts cooperatively with the N-terminal BTB domain (weak interaction) in condensate
439 formation (Fig. 4A), consistent with the finding that membrane-less assemblies can be formed
440 by an ensemble of low-affinity molecular interactions (Boija *et al*, 2018). Since interaction
441 partners of NPH3 that are essential for condensate formation have not yet been identified
442 (Table EV1) (Sullivan *et al*, 2021), we suspected NPH3 to form a single-component
443 condensate. Consequently, LIP-mediated self-association of NPH3 at the PM appears to be
444 coupled to weak BTB-mediated homo-oligomerization in the cytosol, facilitating the
445 formation of higher-order complexes. Based on the AF2M prediction, the BTB domain
446 (NPH3ΔC164 without the bipartite C-terminal motif) may facilitate antiparallel dimerization
447 (Fig. EV4B). This process would lead to the formation of crosslinked and rotated trimers,
448 ultimately resulting in a 3D network of polymerized trimers in the cytosol (Figs. 4D and
449 EV4C). However, the 3D arrangement of the individual trimers also influences the
450 positioning of the phospholipid-binding motif, potentially hindering effective binding on the
451 2D space of the PM. We therefore propose that this affine phospholipid binding restricts
452 higher-order 3D oligomerization via weak BTB-BTB interactions at the PM. In summary,
453 NPH3 acts as a bistable switch regulated by its subcellular localization. Here, a strict C-
454 terminal trimerization at the PM is transformed into a co-operative bivalent (LIP and BTB)
455 homo-oligomerization in the 3D space of the cytosol.
456 During eukaryotic evolution, BTB domains progressively adapted to fulfill diverse cellular
457 functions (Emenecker *et al*, 2021; Field *et al*, 2023). NRL family members are plant-specific
458 BTB domain proteins and feature a conserved extension at the C-terminus of the BTB domain
459 (α6 - α8) (Bonchuk *et al*, 2023), which is crucial for condensate assembly of NPH3 (Fig. 4E).
460 In addition, the NRL BTB domains adopted an N-terminal extension (Bonchuk *et al*, 2023)
461 with high structural variability among NRL family members. These variations could affect the
462 ability, strength and orientation of BTB homo-oligomerization. It is worth noting that NPH3
463 may form part of a CULLIN3 RING E3 UBIQUITIN LIGASE (CRL3) (Roberts *et al*, 2011).
464 Several – non NRL - plant BTB domain proteins act as substrate adapters in CRL3s with the
465 BTB domain responsible for binding to the scaffold CULLIN3 (CUL3) (Ban & Estelle,
466 2021). BTB dimerization by apposition of two monomers in the same orientation is important
467 for the function of many CRL3 orthologues in humans/yeast. Such BTB dimer formation is
468 unlikely for NPH3 (Bonchuk *et al*, 2023) (Fig. EV4B) and CUL3 was not identified as an

469 NPH3 interaction partner in transgenic plants (EV Table1) (Sullivan *et al*, 2021). Clearly,
470 further biochemical work is needed to elucidate the possible involvement of NRL BTB
471 domains in protein ubiquitylation. Variations in the N-terminal extension of NRL BTB
472 domains could furthermore impact on homo-oligomerization of NRLs in general (CC/LIP
473 *versus* BTB). NRL family members lacking a stringent CC domain might therefore rely either
474 on the BTB domain or the LIP motif for homo-oligomerization, depending on their respective
475 affinities. In this context, NPY8/NRL5 which localizes close to the PM and belongs to a
476 different NRL clade, was recently described to homomerize via its BTB domain based on *in*
477 *vitro* pull-down assays (Upadhyay-Tiwari *et al*, 2024). Conversely, both the homo-
478 oligomerization of NPH3 at the PM (Fig. 1C) and its interaction with RPT2 (Fig. 6B) occurs
479 independently of its BTB domain *in planta*. Interestingly, AF2M predicts NPY8/NRL5 to
480 form either a BTB-mediated dimer or alternatively a LIP-mediated trimer. It is therefore of
481 importance to validate these scenarios experimentally, taking into account possible changes in
482 subcellular localization.
483 The use of biomolecular condensates as a means of spatial and temporal regulation is a
484 ubiquitous phenomenon observed in all kingdoms of life. Plant biomolecular condensates are
485 increasingly recognized as playing important roles in plant development and environmental
486 responses. Prominent examples encompass flowering, auxin signaling, seed germination,
487 RNA processing and immunity (Emenecker *et al*, 2021; Field *et al*, 2023). Reversible protein
488 assemblies are usually drivers of either recruitment or sequestration. Sequestration of the
489 auxin response factor ARF19 into cytosolic condensates regulates auxin transcriptional
490 responses in a cell-specific manner by keeping the transcription factor away from the nucleus
491 (Powers *et al*, 2019). Regarding NPH3, transitioning into a condensed state likely sequesters
492 the protein in the cytosol, thereby regulating its rate of re-association with the PM, which can
493 be observed not only upon re-transfer to darkness (Reuter *et al*, 2021) but also upon
494 prolonged irradiation (Haga *et al*, 2015). Mutations that disrupt NPH3 condensates almost
495 completely abolished phototropic hypocotyl bending (Fig. 6A), suggesting that a precise
496 dwell time of NPH3 in the cytosol is critical for function. However, we cannot rule out the
497 possibility that the limited function of these variants is due to loss of an essential interaction
498 that requires the C-terminal extension of the BTB domain of NPH3. Such an *in vivo*
499 interaction partner has, however, not yet been identified (EV Table1) (Sullivan *et al*, 2021).
500 Overall, our data suggest that phase separation provides a mechanism to regulate cycling of
501 NPH3 between the PM and the cytosol, particularly temporally. The elucidation of a putative
502 important function of NPH3 at the PM, which must be modified in a transient and temporally
503 tightly controlled manner to trigger phototropic hypocotyl bending, represents a major
504 challenge for future research.
505
506 **Material and Methods**
507 **Plant materials, transformation and growth conditions**
508 Seeds of *Arabidopsis thaliana* [ecotype Columbia-0 (Col-0), *nph3-7* (SALK_110039, Col-0
509 background)] were obtained from the Nottingham Arabidopsis Stock Centre, and the *nph3-7*
510 transgenic lines expressing GFP:NPH3 or GFP:NPH3ΔC51 have been described recently
511 (Reuter *et al*, 2021). Stable transformation of *nph3-7* followed standard procedures.
512 Unless otherwise stated, seeds were surface sterilized and plated on solid half-strength
513 Murashige and Skoog (MS) medium (pH 5.8) containing 1 % sucrose (w/v). Following
514 stratification in the dark for 48-72 h at 4°C, seeds were exposed to fluorescent white light for
515 4 h. Seedlings were then grown in darkness for 68 h at 20°C. Subsequently, the etiolated
516 seedlings were either kept in darkness or irradiated with BL [overhead BL (1 μmol $m^{-2}s^{-1}$) for
517 up to 1 hour or, alternatively, GFP-laser treatment (488 nm) for up to 11 min during confocal
518 observation, as specified in the Figure legends]. Independent experiments were carried out at
519 least in triplicates. Representative images are presented.

520 *Agrobacterium*-mediated transient transformation of 3-4 weeks old *Nicotiana benthamiana*
521 plants was performed as described previously (Blatt & Grefen, 2014). *Agrobacterium*
522 *tumefaciens* strain GV3101, transformed with a binary vector of interest, was resuspended in
523 infiltration solution (10 mM MES, pH 5.6, 10 mM $MgCl_2$, 150 µM acetosyringone) at an
524 OD_{600} of 0.1 – 0.2 and syringe-infiltrated into the abaxial epidermis of *N. benthamiana* leaves.
525 For co-transformation, a 1:1 mixture was used, sometimes combined with co-introduction of a
526 suppressor of post-transcriptional gene silencing [35S::P19 (Win & Kamoun, 2004), OD_{600}:
527 0.01 – 0.05]. Freshly transformed tobacco plants were kept under constant light for 24 h,
528 subsequently transferred to darkness for 17 h (dark adaptation) and finally either kept in
529 darkness (D) or BL-irradiated [overhead BL (10 µmol $m^{-2}s^{-1}$) for up to 1 hour or,
530 alternatively, the GFP-laser treatment (488 nm) for up to 11 min during confocal inspection of
531 abaxial leaf epidermis cells, as specified in the Figure legends]. Independent experiments
532 were carried out at least in triplicates. Representative images are presented.
533
534 **Cloning procedures**
535 Cloning of N-terminally fluorophore-tagged NPH3 variants (GFP and/or RFP) into the
536 destination vectors pB7WGR2 and/or pH7WGF2 (Karimi *et al*, 2007) for stable
537 transformation or transient overexpression followed standard GATEWAY™ procedures. The
538 35S-driven NPH3 variants GFP/RFP:NPH3, GFP/RFP:NPH3_S744A, GFP/RFP:NPH3ΔC51
539 and GFP/RFP:NPH3_4K/A transformation vectors have been described before (Reuter *et al*,
540 2021). Transgenic plants were selected based on the hygromycin resistance conferred by
541 pH7WGF2 and homozygous lines were established.
542 Site-directed mutagenesis was performed by PCR, while deletions were generated by primer
543 extension PCR. PCR products and products of mutagenesis were verified by sequencing. A
544 complete list of oligonucleotides used in this study for PCR is provided in EV Table 2.
545
546 **Expression and purification of proteins**
547 For bacterial expression of the Arabidopsis C-terminal NPH3 variants N-terminally tagged
548 with $(His)_6$-Maltose Binding Protein (MBP), the corresponding cDNA was amplified by PCR
549 and cloned into the expression vector pDEST-HisMBP (Addgene plasmid #11085) using
550 standard GATEWAY™ procedures. Recombinant NPH3 proteins were expressed using
551 *Escherichia coli* BL21(DE3) host strain. Transformed *E.coli* BL21(DE3) was grown in liquid
552 2 x yeast extract and tryptone (2YT) medium containing ampicillin (100 µg/ml) at 37°C until
553 an OD_{600} of 0.6. Protein expression was induced by adding IPTG to a final concentration of
554 0.5 mM. Following overnight growth at 16°C, bacteria were harvested by centrifugation
555 (4000 rpm, 30 min, 4 °C). The pellet was frozen in liquid nitrogen. Following thawing on ice
556 the cells were resuspended in bacterial protein extraction reagent B-PER (5 ml/g fresh weight)
557 (Thermo Scientific, Waltham, USA) supplemented with Protease Inhibitor Mix-B (Serva,
558 Heidelberg, Germany). Purification under native conditions was done by using the cleared
559 BL21(DE3) lysate and Ni^{2+}-NTA agarose (Qiagen, Hilden, Germany) according to the
560 manufacturer's protocol.
561
562 **Size Exclusion Chromatography (SEC)**
563 SEC was performed using the Superdex 200 Increase 10/300 GL column in combination with
564 the ÄKTA™ pure chromatography system (Cytiva, Marlborough, USA). 200 µl of purified
565 recombinant protein (approx. 2 mg/ml) was loaded onto the PBS-equilibrated (10 mM
566 phosphate buffer, 140 mM NaCl, pH 7.4) column using a flow rate of 0.1 ml/min
567 (UNICORN™ 7.0 program, Cytiva), and collected in 0.5 ml fractions using a 96-well fraction
568 collector (Biozym, Oldendorf, Germany). The collected fractions were subjected to
569 immunoblot analysis. The molecular weight of the recombinant NPH3 proteins was calibrated
570 using standard size protein markers [High Molecular Weight Gel Filtration Calibration Kit

571 (Cytiva): thyroglobulin (669 kDa, 5 mg/ml), Ferritin (440 kDa, 0.3 mg/ml), Aldolase (158
572 kDa, 4 mg/ml), Conalbumin (75 kDa, 3 mg/ml), Albumin (44 kDa, 4 mg/ml) and
573 Chymotrypsinogen A (25 kDa, 3 mg/ml)].
574
575 **Preparation of microsomal membranes**
576 Microsomal membrane fractions were prepared from transiently transformed and dark-
577 adapted *N. benthamiana* leaves. Tissue was homogenized with 3 ml of ice-cold
578 homogenization buffer per g fresh weight [50 mM Hepes, pH 7.8, 500 mM sucrose, 1 % PVP-
579 40, 3 mM dithiothreitol (DTT), 3 mM EDTA, supplemented with Complete Protease Inhibitor
580 Mixture (Roche, Basel, Switzerland) and Phosphatase Inhibitor Mix 1 (Serva)]. The
581 homogenate was centrifuged at 10,000 × g for 20 min at 4°C. The supernatant was filtered
582 through MiraCloth and subsequently centrifuged at 100,000 × g for 45 min at 4°C. The
583 microsomal pellet was resuspended in ice-cold 5 mM Tris/MES, pH 6.5, 330 mM sucrose, 2
584 mM DTT, supplemented with Complete Protease Inhibitor Mixture (Roche) and Phosphatase
585 Inhibitor Mix 1 (Serva). All the above steps were performed under red safe light conditions.
586
587 **Co-Immunoprecipitation and MS analysis**
588 *In vivo* interaction of fluorophore-tagged NPH3 variants was tested by using total plant
589 protein extracts obtained from transiently transformed *N. benthamiana* leaves according to
590 (Albert *et al*, 2015) with slight modifications. Dark-adapted tobacco plants were either kept in
591 darkness or treated with overhead BL (10 µmol $m^{-2}s^{-1}$) for 1 h. Approximately 500 mg of leaf
592 tissue was ground thoroughly under red safe light illumination and suspended in solubilization
593 buffer [50 mM Tris, pH 7.5, 150 mM NaCl, 1 mM EDTA, 0.75% Triton X-100 supplemented
594 with Complete Protease Inhibitor Mixture (Roche) and Phosphatase Inhibitor Mix 1 (Serva)].
595 After 1 h incubation on an overhead rotor at 4 °C, cell debris-removed supernatant was
596 incubated with equilibrated 20 µl GFP-Trap® or RFP-Trap® agarose beads (ChromoTek and
597 Proteintech Company, Planegg-Martinsried, Germany) for 1 h in the cold room with overhead
598 rotation. The beads were washed three times with solubilization buffer containing 0.1% Triton
599 X-100, followed by a final washing step using 50 mM Tris, pH 7.5, 150 mM NaCl. Finally,
600 proteins were eluted by adding 40 µl of 2 × SDS sample buffer (100 mM Tris-HCl, pH 6.8,
601 20% glycerol, 2% β-Mercaptoethanol, 4% SDS, 0.02% bromophenol blue) and boiling at 95
602 °C for 10 min. The denatured proteins were subsequently separated by SDS-PAGE.
603 Arabidopsis *nph3-7* ectopically expressing GFP:NPH3 and, as control, GFP (UBQ10
604 promoter) were sown on half-strength MS plates and grown in the dark for 3 days.
605 Subsequently, the etiolated seedlings were either kept in darkness or treated with overhead BL
606 (1 µmolm^{-2} s^{-1}) for 30min. Three grams of plant tissue were used under red safe light
607 illumination for immunoprecipitation essentially as described above. Cell debris-removed
608 supernatants were incubated with 50 µl GFP-Trap beads (ChromoTek) for 3 h in the cold
609 room with mild rotation. The washing steps were supplemented by a final wash (3x) with
610 20mM ammoniumbicarbonate buffer. On-beads digestion with trypsin, peptide purification
611 with Phoenix kit (PreOmics) and liquid chromatography-MS/MS analysis (Proxeon Easy-nLC
612 coupled to an QExactiveHF-X mass spectrometer, Thermo) were performed by the Proteome
613 Center Tübingen, University of Tübingen, essentially as described (Schmitt *et al*, 2021),
614 except that peptides with a resolution of 45,000 were selected for MS/MS sequencing.
615
616 **Protein quantification, SDS-PAGE and Western Blotting**
617 Protein concentration was determined using ROTI® Nanoquant (Carl Roth, Karlsruhe,
618 Germany) according to the manufacturer's protocol.
619 SDS-PAGE, Western blotting and immunodetection followed standard procedures. Total
620 proteins were extracted from transiently transformed *N. benthamiana* leaves (2 leaf discs) by
621 directly grinding in 100 µl 2 × SDS sample buffer under red safe light illumination.

622 Total protein extracts from 3-day-old etiolated Arabidopsis seedlings (150 seedlings) were
623 prepared by grinding the frozen tissue in ice-cold extraction buffer (20 mM Tris, pH 7.0, 150
624 mM NaCl, 1 mM EDTA, 1 % Triton X-100, 0.1 % SDS, 5 mM DTT) supplemented with
625 Complete Protease Inhibitor Mixture (Roche) and Phosphatase Inhibitor Mix I (Serva). After
626 10 minutes incubation on ice, cell debris-removed supernatants were used for
627 immunodetection. Chemiluminescence was detected using an Amersham ImageQuant 800
628 (Cytiva) system. Images were processed with Adobe Photoshop CS5 (Adobe Inc., San José,
629 CA, USA) for adjustment of brightness and contrast. Chemiluminescence detection was
630 performed using the ECL™ Prime Western Blot Detection Reagent (Cytiva).
631 The following antibodies were used in this study: anti-NPH3-S744P (Reuter *et al*, 2021)
632 (1:500), anti-NPH3 (Reuter *et al*, 2021) (1:1000) , anti-GFP (1:1000, Thermo Scientific,
633 catalog number: A-11122, lot: 2477546), anti-RFP 5F8 (1:1000, ChromoTek and Proteintech
634 Company, catalog number: 5f8-150, lot: 104272-05), anti-His_6 (1:2000, Roche/Merck,
635 Darmstadt, Germany, catalog no: 11965085001).
636
637 **Hypocotyl Phototropism analysis**
638 Phototropism was performed using *A. thaliana* seedlings which were grown in the dark for 72
639 h on vertically oriented solid half-strength MS plates containing 1 % sucrose. Etiolated
640 seedlings were then transferred to a LED chamber and illuminated with unilateral BL (0.1
641 $\mu mol\ m^{-2}\ s^{-1}$) for 24 h. Plates were scanned, and the inner hypocotyl angle was measured for
642 each seedling using ImageJ (Schindelin *et al*, 2012). The curvature angle was calculated as
643 the difference between 180° and the measured value. For each transgenic line three biological
644 replicates ($n \geq 30$ seedlings per experiment) were performed, alongside with the appropriate
645 controls (Col-0, *nph3-7*).
646
647 **AlphaFold Predictions**
648 To predict protein and protein complex structures we used the AlphaFold2-Multimer program
649 developed by Google DeepMind (Evans *et al*, 2022; Jumper *et al*, 2021) through a
650 subscription to the Google Colab v1.5.5 (Mirdita *et al*, 2022)
651 (https://colab.research.google.com/github/sokrypton/ColabFold/blob/main/AlphaFold2.ipynb)
652 following guidelines on the document. As an alternative, AF3 predictions (developed by
653 Google DeepMind and Isomorphic Labs) (Abramson *et al*, 2024) were generated via the
654 newly launched AlphaFold server (https://alphafoldserver.com). Models were colored in
655 PyMol (The PyMOL Molecular Graphics System, Version 2.5.8 Schrödinger, LLC). Where
656 indicated, predictions are colored according to the AF2 produced per-residue confidence
657 metric called the local distance difference test (pLDDT) (Elfmann & Stülke, 2023; Evans *et*
658 *al*, 2022) via visualization in PyMol.
659
660 **Confocal microscopy**
661 Live-cell imaging was performed using the Leica TCS SP8 (upright) confocal laser scanning
662 microscope. Imaging was done by using a 63x/1.20 water immersion objective. For excitation
663 and emission of fluorophores, the following laser settings were used: GFP, excitation 488 nm,
664 emission 505-530 nm; RFP, excitation 558 nm, emission 600-630 nm. All CLSM images in a
665 single experiment were captured with the same settings using the Leica Confocal Software.
666 For simultaneous imaging of samples expressing two fluorophores, sequential scanning mode
667 was used supported by Leica Confocal Software. All experiments were repeated at least three
668 times. Both the focal plane images and Z-stack maximum projection images were processed
669 using Leica Application Suite X 3.7.4.23463.
670 For *in planta* FRET-FLIM analyses, *N. benthamiana* plants were analyzed 2 days after
671 transient transformation using an SP8 confocal laser scanning microscope (Leica
672 Microsystems), which was equipped with the Leica Microsystems Application Suite software

673 and a FastFLIM upgrade from PicoQuant (Sepia multichannel picosecond diode laser,
674 PicoQuant TimeHarp 260 TCSPC module, and Picosecond Event Timer). The measurements
675 were performed according to (Ladwig *et al*, 2015) and (Glöckner *et al*, 2022) with some
676 adjustments. Imaging was performed using a 63x/1.20 water-immersion objective, focusing
677 on the PM of abaxial epidermal cells. Prior to the FRET-FLIM measurements, the presence of
678 the fluorophore-fusions was confirmed by using 488 or 561 nm lasers for excitation of GFP or
679 RFP, respectively. The donor lifetime was determined in donor-only expressing cells or cells
680 with the indicated combinations using a pulsed laser as an excitation light source at 470 nm
681 and a repetition rate of 40 MHz. The acquisition was performed until 500 photons were
682 reached in the brightest pixel, with a resolution of 256 x 256 pixels and a pixel dwell time of
683 ~ 20 µs. The corresponding emission was detected with a HyD SMD from 500 nm to 550 nm
684 by TCSPC.
685 For condensate analyses in vivo, 4-day-old seedlings grown on half-strength MS plates
686 supplemented with 1 % sucrose were transferred on a microscopy slide with either water or
687 10% 1,6-hexanediol (Merck, 240117), supplemented with 3 µg/ml propidium iodide for
688 viability test, immediately before imaging. Root epidermal cells were analyzed 3 min after
689 treatment. For counting the number of puncta, a threshold was set for each image, the images
690 were converted to binary images, and masked. Region of Interests with uniform fluorescence
691 were selected and the number of particles was counted using the "Analyze Particles" function
692 in Fiji with 0.05/0.1 to 8/10 μm^2 as size range and 0 to 1 circularity. The number of puncta
693 was then normalized for the area of 10000 µm2.
694
695 **Data analysis**
696 For all semi-quantitative CoIPs, the protein band intensities of GFP and RFP from IP:GFP
697 were determined by Western blot quantification using ImageJ software as described by
698 Hossein Davarinejad (http://www.yorku.ca/yisheng/Internal/Protocols/ImageJ.pdf). As a next
699 step, the ratio of RFP band intensity to the corresponding GFP band intensity was determined.
700 The values given in Fig. 2B were normalized to NPH3WT/NPH3ΔC104 (dark; left panel) and
701 NPH3_WLM_E/NPH3ΔC51 (dark; right panel). Likewise, the values in Fig. EV2B were
702 normalized to NPH3ΔC51/NPH3ΔC104 (dark).
703 FRET-FLIM: The SymPhoTime 64 software (Vers. 2.9) was employed for data processing.
704 Iterative reconvolution was used to calculate the FLTs, i.e. the instrument response function
705 was convolved with a bi-exponential decay function, for both the donor-only expressing cells
706 and the indicated combinations. Only the range between 1.3 ns and 20 ns was used for fitting.
707 To calculate the percentage of IPS in FRET-FLIM measurements we made use of
708 custom-made R-Scripts and set adjusted thresholds according to (Bücherl *et al*, 2013). The
709 scripts will be made accessible upon completion of the peer-review process or upon request.
710 The photon counts per pixel must be at least 250. For each pixel that met the aforementioned
711 criterion, the FLT was derived by intensity-weighted averaging and the values were exported
712 from the SymPhoTime 64 software. For further processing, pixels with FLTs below 1.5 and
713 above 2.7 were excluded to avoid false positive or negative interactions. Subsequently, the
714 mean FLT of all donor-only samples were determined. Based on this value and the threshold
715 of 10 % FRET efficiency (Glöckner *et al*, 2022), the limit of IPS was defined. According to
716 this definition, all cells were analyzed and only pixels with FLTs below the interaction
717 threshold were collected as IPS. The ratio between the IPS and the total amount of selected
718 pixels represents the value of IPS in the respective graph.
719 IP-MS: Processing of the data was conducted using MaxQuant software (vs 2.2.0.0.). The
720 spectra were searched against an *A. thaliana* UniProt database. Raw data processing was done
721 with 1% false discovery rate setting. Two individual biological replicates were performed and
722 mitochondrial, chloroplastic and peroxisomal proteins were omitted from the list of GFP-
723 NPH3 interaction partners. Only proteins identified in two biological replicates from at least

two peptides were retained for analysis. Proteins identified in IPs from GFP-expressing seedlings (≥ 3 peptides or number of peptides close to the bait) were considered contaminants. Protein Intensity-Based Absolute Quantification values (iBAQ) were converted to normalized iBAQ of the bait protein (GFP:NPH3). Proteins showing at least a twofold change in iBAQ values following blue light irradiation were identified (Table EV1).

The number of condensates from seedlings expressing GFP:NPH3ΔC51 was analyzed using ImageJ software (see confocal microscopy). Graphical and statistical analysis (two-tailed unpaired *t*-test with unequal variance) were performed using the software GraphPad Prism. Error bars represent SD.

The angles of phototropic curvature of all analyzed Arabidopsis genotypes (≥ 30 seedlings per genotype per replicate) were measured using ImageJ software. Graphical analysis was performed using the software GraphPad Prism. Statistical significance of the data was assessed using one-way ANOVA followed by *post hoc* Tukey multiple comparison test ($P < 0.05$). Error bars represent SD.

References

Abramson J, Adler J, Dunger J, Evans R, Green T, Pritzel A, Ronneberger O, Willmore L, Ballard AJ, Bambrick J *et al* (2024) Accurate structure prediction of biomolecular interactions with AlphaFold 3. *Nature*

Albert I, Böhm H, Albert M, Feiler CE, Imkampe J, Wallmeroth N, Brancato C, Raaymakers TM, Oome S, Zhang H *et al* (2015) An RLP23–SOBIR1–BAK1 complex mediates NLP-triggered immunity. *Nat Plants* 1: 15140

Ban Z, Estelle M (2021) CUL3 E3 ligases in plant development and environmental response. *Nat Plants* 7: 6-16

Banani SF, Lee HO, Hyman AA, Rosen MK (2017) Biomolecular condensates: organizers of cellular biochemistry. *Nat Rev Mol Cell Biol* 18: 285-298

Blatt MR, Grefen C (2014) Applications of fluorescent marker proteins in plant cell biology. *Methods Mol Biol* 1062: 487-507

Boija A, Klein IA, Sabari BR, Dall'Agnese A, Coffey EL, Zamudio AV, Li CH, Shrinivas K, Manteiga JC, Hannett NM *et al* (2018) Transcription Factors Activate Genes through the Phase-Separation Capacity of Their Activation Domains. *Cell* 175: 1842-1855.e1816

Bonchuk A, Balagurov K, Georgiev P (2023) BTB domains: A structural view of evolution, multimerization, and protein-protein interactions. *Bioessays* 45: e2200179

Bücherl CA, van Esse GW, Kruis A, Luchtenberg J, Westphal AH, Aker J, van Hoek A, Albrecht C, Borst JW, de Vries SC (2013) Visualization of BRI1 and BAK1(SERK3) Membrane Receptor Heterooligomers during Brassinosteroid Signaling *Plant Physiology* 162: 1911-1925

Cheng Y, Qin G, Dai X, Zhao Y (2007) NPY1, a BTB-NPH3-like protein, plays a critical role in auxin-regulated organogenesis in Arabidopsis. *Proc Natl Acad Sci U S A* 104: 18825-18829

Christie JM, Murphy AS (2013) Shoot phototropism in higher plants: new light through old concepts. *Am J Bot* 100: 35-46

Christie JM, Suetsugu N, Sullivan S, Wada M (2018) Shining Light on the Function of NPH3/RPT2-Like Proteins in Phototropin Signaling. *Plant Physiol* 176: 1015-1024

Ding Z, Galván-Ampudia CS, Demarsy E, Łangowski Ł, Kleine-Vehn J, Fan Y, Morita MT, Tasaka M, Fankhauser C, Offringa R *et al* (2011) Light-mediated polarization of the PIN3 auxin transporter for the phototropic response in Arabidopsis. *Nat Cell Biol* 13: 447-452

Dolde U, Muzzopappa F, Delesalle C, Neveu J, Erdel F, Vert G (2023) LEAFY homeostasis is regulated via ubiquitin-dependent degradation and sequestration in cytoplasmic condensates. *iScience* 26: 106880

Elfmann C, Stülke J (2023) PAE viewer: a webserver for the interactive visualization of the predicted aligned error for multimer structure predictions and crosslinks. *Nucleic Acids Res* 51: W404-W410

Emenecker RJ, Holehouse AS, Strader LC (2021) Biological Phase Separation and Biomolecular Condensates in Plants. *Annu Rev Plant Biol* 72: 17-46

Evans R, O'Neill M, Pritzel A, Antropova N, Senior A, Green T, Žídek A, Bates R, Blackwell S, Yim J *et al* (2022) Protein complex prediction with AlphaFold-Multimer. *bioRxiv*: 2021.2010.2004.463034

Fankhauser C, Christie JM (2015) Plant phototropic growth. *Curr Biol* 25: R384-389
Field S, Jang G-J, Dean C, Strader LC, Rhee SY (2023) Plants use molecular mechanisms mediated by biomolecular condensates to integrate environmental cues with development. *The Plant Cell* 35: 3173-3186
Furutani M, Kajiwara T, Kato T, Treml BS, Stockum C, Torres-Ruiz RA, Tasaka M (2007) The gene MACCHI-BOU 4/ENHANCER OF PINOID encodes a NPH3-like protein and reveals similarities between organogenesis and phototropism at the molecular level. *Development* 134: 3849-3859
Furutani M, Sakamoto N, Yoshida S, Kajiwara T, Robert HS, Friml J, Tasaka M (2011) Polar-localized NPH3-like proteins regulate polarity and endocytosis of PIN-FORMED auxin efflux carriers. *Development* 138: 2069-2078
Glanc M, Van Gelderen K, Hoermayer L, Tan S, Naramoto S, Zhang X, Domjan D, Včelařová L, Hauschild R, Johnson A *et al* (2021) AGC kinases and MAB4/MEL proteins maintain PIN polarity by limiting lateral diffusion in plant cells. *Curr Biol*
Glöckner N, zur Oven-Krockhaus S, Rohr L, Wackenhut F, Burmeister M, Wanke F, Holzwart E, Meixner AJ, Wolf S, Harter K (2022) Three-Fluorophore FRET Enables the Analysis of Ternary Protein Association in Living Plant Cells. *Plants* 11: 2630
Haga K, Sakai T (2023) Photosensory adaptation mechanisms in hypocotyl phototropism: how plants recognize the direction of a light source. *J Exp Bot* 74: 1758-1769
Haga K, Takano M, Neumann R, Iino M (2005) The Rice COLEOPTILE PHOTOTROPISM1 gene encoding an ortholog of Arabidopsis NPH3 is required for phototropism of coleoptiles and lateral translocation of auxin. *Plant Cell* 17: 103-115
Haga K, Tsuchida-Mayama T, Yamada M, Sakai T (2015) Arabidopsis ROOT PHOTOTROPISM2 Contributes to the Adaptation to High-Intensity Light in Phototropic Responses. *Plant Cell* 27: 1098-1112
Hohm T, Preuten T, Fankhauser C (2013) Phototropism: translating light into directional growth. *Am J Bot* 100: 47-59
Inada S, Ohgishi M, Mayama T, Okada K, Sakai T (2004) RPT2 is a signal transducer involved in phototropic response and stomatal opening by association with phototropin 1 in Arabidopsis thaliana. *Plant Cell* 16: 887-896
Jumper J, Evans R, Pritzel A, Green T, Figurnov M, Ronneberger O, Tunyasuvunakool K, Bates R, Žídek A, Potapenko A *et al* (2021) Highly accurate protein structure prediction with AlphaFold. *Nature* 596: 583-589
Karimi M, Depicker A, Hilson P (2007) Recombinational cloning with plant gateway vectors. *Plant Physiol* 145: 1144-1154
Kimura T, Haga K, Nomura Y, Higaki T, Nakagami H, Sakai T (2021) Phosphorylation of NONPHOTOTROPIC HYPOCOTYL3 affects photosensory adaptation during the phototropic response. *Plant Physiol*
Küpers JJ, Oskam L, Pierik R (2020) Photoreceptors Regulate Plant Developmental Plasticity through Auxin. *Plants (Basel)* 9
Ladwig F, Dahlke RI, Stührwohldt N, Hartmann J, Harter K, Sauter M (2015) Phytosulfokine Regulates Growth in Arabidopsis through a Response Module at the Plasma Membrane That Includes CYCLIC NUCLEOTIDE-GATED CHANNEL17, H+-ATPase, and BAK1. *The Plant Cell* 27: 1718-1729
Legris M, Boccaccini A (2020) Stem phototropism toward blue and ultraviolet light. *Physiol Plant* 169: 357-368
Li Y, Dai X, Cheng Y, Zhao Y (2011) NPY genes play an essential role in root gravitropic responses in Arabidopsis. *Mol Plant* 4: 171-179
Lyon AS, Peeples WB, Rosen MK (2021) A framework for understanding the functions of biomolecular condensates across scales. *Nat Rev Mol Cell Biol* 22: 215-235
Martinez D, Legrand A, Gronnier J, Decossas M, Gouguet P, Lambert O, Berbon M, Verron L, Grélard A, Germain V *et al* (2019) Coiled-coil oligomerization controls localization of the plasma membrane REMORINs. *J Struct Biol* 206: 12-19
Mirdita M, Schütze K, Moriwaki Y, Heo L, Ovchinnikov S, Steinegger M (2022) ColabFold: making protein folding accessible to all. *Nat Methods* 19: 679-682

832 Mosesso N, Lerner NS, Bläske T, Groh F, Maguire S, Niedermeier ML, Landwehr E, Vogel K,
833 Meergans K, Nagel M-K *et al* (2024) Arabidopsis CaLB1 undergoes phase separation with the
834 ESCRT protein ALIX and modulates autophagosome maturation. *Nature communications* 15: 5188
835 Motchoulski A, Liscum E (1999) *Arabidopsis* NPH3: A NPH1 Photoreceptor-Interacting Protein
836 Essential for Phototropism. *Science* 286: 961-964
837 Pedmale UV, Celaya RB, Liscum E (2010) Phototropism: mechanism and outcomes. In: *Arabidopsis*
838 *Book*, p. e0125.
839 Pedmale UV, Liscum E (2007) Regulation of phototropic signaling in Arabidopsis via
840 phosphorylation state changes in the phototropin 1-interacting protein NPH3. *J Biol Chem* 282:
841 19992-20001
842 Powers SK, Holehouse AS, Korasick DA, Schreiber KH, Clark NM, Jing H, Emenecker R, Han S,
843 Tycksen E, Hwang I *et al* (2019) Nucleo-cytoplasmic Partitioning of ARF Proteins Controls Auxin
844 Responses in Arabidopsis thaliana. *Mol Cell* 76: 177-190.e175
845 Reuter L, Schmidt T, Manishankar P, Throm C, Keicher J, Bock A, Droste-Borel I, Oecking C (2021)
846 Light-triggered and phosphorylation-dependent 14-3-3 association with NON-PHOTOTROPIC
847 HYPOCOTYL 3 is required for hypocotyl phototropism. *Nat Comm* 12: 6128
848 Roberts D, Pedmale UV, Morrow J, Sachdev S, Lechner E, Tang X, Zheng N, Hannink M, Genschik
849 P, Liscum E (2011) Modulation of Phototropic Responsiveness in Arabidopsis through Ubiquitination
850 of Phototropin 1 by the CUL3-Ring E3 Ubiquitin Ligase CRL3NPH3 *The Plant Cell* 23: 3627-3640
851 Schindelin J, Arganda-Carreras I, Frise E, Kaynig V, Longair M, Pietzsch T, Preibisch S, Rueden C,
852 Saalfeld S, Schmid B *et al* (2012) Fiji: an open-source platform for biological-image analysis. *Nat*
853 *Methods* 9: 676-682
854 Schmitt M, Sinnberg T, Niessner H, Forschner A, Garbe C, Macek B, Nalpas NC (2021)
855 Individualized proteogenomics reveals mutational landscape of melanoma patients in response to
856 immunotherapy. *Cancers* 13: 5411
857 Shin Y, Brangwynne CP (2017) Liquid phase condensation in cell physiology and disease. *Science*
858 357
859 Stogios PJ, Downs GS, Jauhal JJ, Nandra SK, Privé GG (2005) Sequence and structural analysis of
860 BTB domain proteins. *Genome Biol* 6: R82
861 Sullivan S, Kharshiing E, Laird J, Sakai T, Christie JM (2019) Deetiolation Enhances Phototropism by
862 Modulating NON-PHOTOTROPIC HYPOCOTYL3 Phosphorylation Status. *Plant Physiol* 180: 1119-
863 1131
864 Sullivan S, Waksman T, Paliogianni D, Henderson L, Lütkemeyer M, Suetsugu N, Christie JM (2021)
865 Regulation of plant phototropic growth by NPH3/RPT2-like substrate phosphorylation and 14-3-3
866 binding. *Nat Commun* 12: 6129
867 Treml BS, Winderl S, Radykewicz R, Herz M, Schweizer G, Hutzler P, Glawischnig E, Ruiz RA
868 (2005) The gene ENHANCER OF PINOID controls cotyledon development in the Arabidopsis
869 embryo. *Development* 132: 4063-4074
870 Tsuchida-Mayama T, Nakano M, Uehara Y, Sano M, Fujisawa N, Okada K, Sakai T (2008) Mapping
871 of the phosphorylation sites on the phototropic signal transducer, NPH3. *Plant Sci* 174: 626-633
872 Upadhyay-Tiwari N, Huang X-J, Lee Y-C, Singh SK, Hsu C-C, Huang S-S, Verslues PE (2024) The
873 nonphototrophic hypocotyl 3 (NPH3) domain protein NRL5 is a trafficking-associated GTPase
874 essential for drought resistance. *Science Advances* 10: eado5429
875 Waksman T, Suetsugu N, Hermanowicz P, Ronald J, Sullivan S, Łabuz J, Christie JM (2023)
876 Phototropin phosphorylation of ROOT PHOTOTROPISM 2 and its role in mediating phototropism,
877 leaf positioning, and chloroplast accumulation movement in Arabidopsis. *Plant J* 114: 390-402
878 Willige BC, Ahlers S, Zourelidou M, Barbosa IC, Demarsy E, Trevisan M, Davis PA, Roelfsema MR,
879 Hangarter R, Fankhauser C *et al* (2013) D6PK AGCVIII kinases are required for auxin transport and
880 phototropic hypocotyl bending in Arabidopsis. *Plant Cell* 25: 1674-1688
881 Win J, Kamoun S (2004) pCB301-p19: A Binary Plasmid Vector to Enhance Transient Expression of
882 Transgenes by Agroinfiltration. http://www.KamounLab.net
883 Zhang Y, Yu Q, Jiang N, Yan X, Wang C, Wang Q, Liu J, Zhu M, Bednarek SY, Xu J *et al* (2017)
884 Clathrin regulates blue light-triggered lateral auxin distribution and hypocotyl phototropism in
885 Arabidopsis. *Plant Cell Environ* 40: 165-176

Zourelidou M, Absmanner B, Weller B, Barbosa IC, Willige BC, Fastner A, Streit V, Port SA, Colcombet J, de la Fuente van Bentem S *et al* (2014) Auxin efflux by PIN-FORMED proteins is activated by two different protein kinases, D6 PROTEIN KINASE and PINOID. *Elife* 3

Acknowledgements
We extend our gratitude to Nathalie Zgoda for her contributions to data analysis, and to Franziska Lanz and Ricarda Furkert for their assistance with the analysis of the recombinant C-terminal NPH3 fusion proteins. We also appreciate the SEC support provided by Chenlei Hua and Lisha Zhang, and the SP8 support from Sandra Richter. Lastly, we thank John Christie and Thorsten Nürnberger for their valuable comments on the manuscript.
Funding: This work was supported by the German Research Foundation (DFG) with a grant to CO (CRC 1101-B09) and grants for scientific equipment (INST 37/819-1 FUGG, INST 37/991-1 FUGG).
Author contributions: CO conceived the project. PM, LRe and CO designed experiments. PM, LRe, LRo, AF, YIY, TS, ID-B, JK and AB performed experiments. CO performed AF2/AF2M/AF3 predictions. PM, LRe, LRo, TS, ID-B and CO analyzed data. The manuscript was principally written by CO with comments from all authors.
Competing interests: The authors declare that they have no competing interests.
Data and materials availability: All data needed to evaluate the conclusions in the paper are present in the paper and/or the Supplementary Materials. Requests for material should be submitted to Claudia Oecking (Email: claudia.oecking@zmbp.uni-tuebingen.de).

907 **FIGURES**

908

909

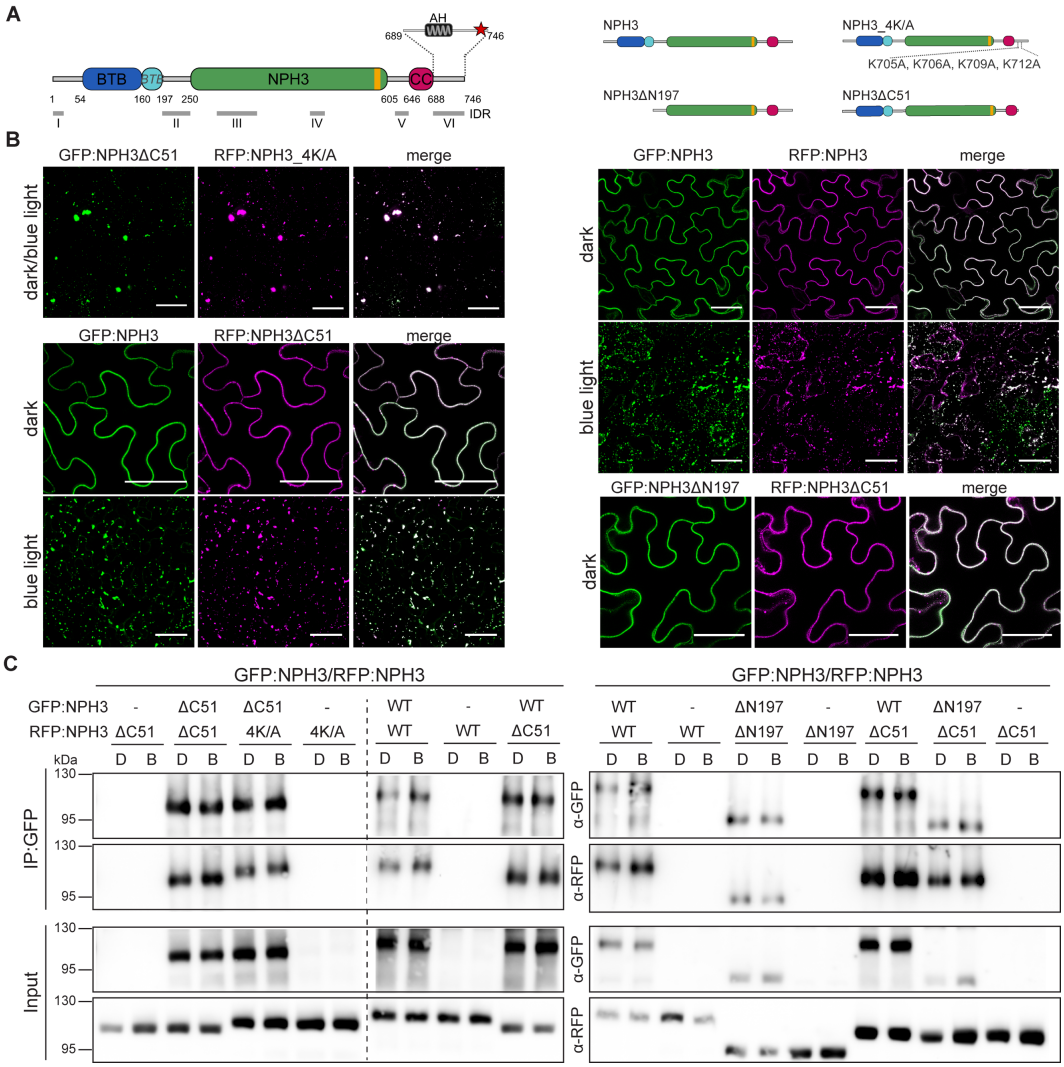

910

911

912 **Figure 1. NPH3 self-associates at the PM and within cytosolic condensates independent of its BTB domain.**
913 (**A**) Domain architecture of NPH3 (746 amino acids) and location of IDRs (AF2 prediction). C-terminal BTB
914 extension highlighted in light blue (*BTB*), LIP motif highlighted in yellow, AH amphipathic helix, see text for
915 details **(left panel).** Schematic representation of NPH3 constructs used **(right panel)**. (**B**) Representative
916 confocal images of leaf epidermal cells from *N. benthamiana* transiently co-expressing different
917 GFP/RFP:NPH3 variants (35S promoter). Dark-adapted tobacco plants were either kept in darkness or treated
918 with BL (~ 11 min GFP laser). Z-stack projections of BL-treated samples are shown. Scale bars, 50 µm. These
919 experiments were repeated at least three times with similar results. (**C**) *In vivo* interaction of GFP/RFP:NPH3
920 variants transiently co-expressed (35S promoter) in *N. benthamiana* leaves. Dark-adapted tobacco plants were
921 either kept in darkness (D) or treated with BL (B) (10 µmol $m^{-2}s^{-1}$, 1h). The crude protein extract was
922 immunoprecipitated using GFP beads. Immunodetection of input and immunoprecipitated proteins (IP:GFP) is
923 shown. Experiments were performed at least two times with similar results. Dotted line indicates that the same
924 blot has been sliced and the sides swapped.

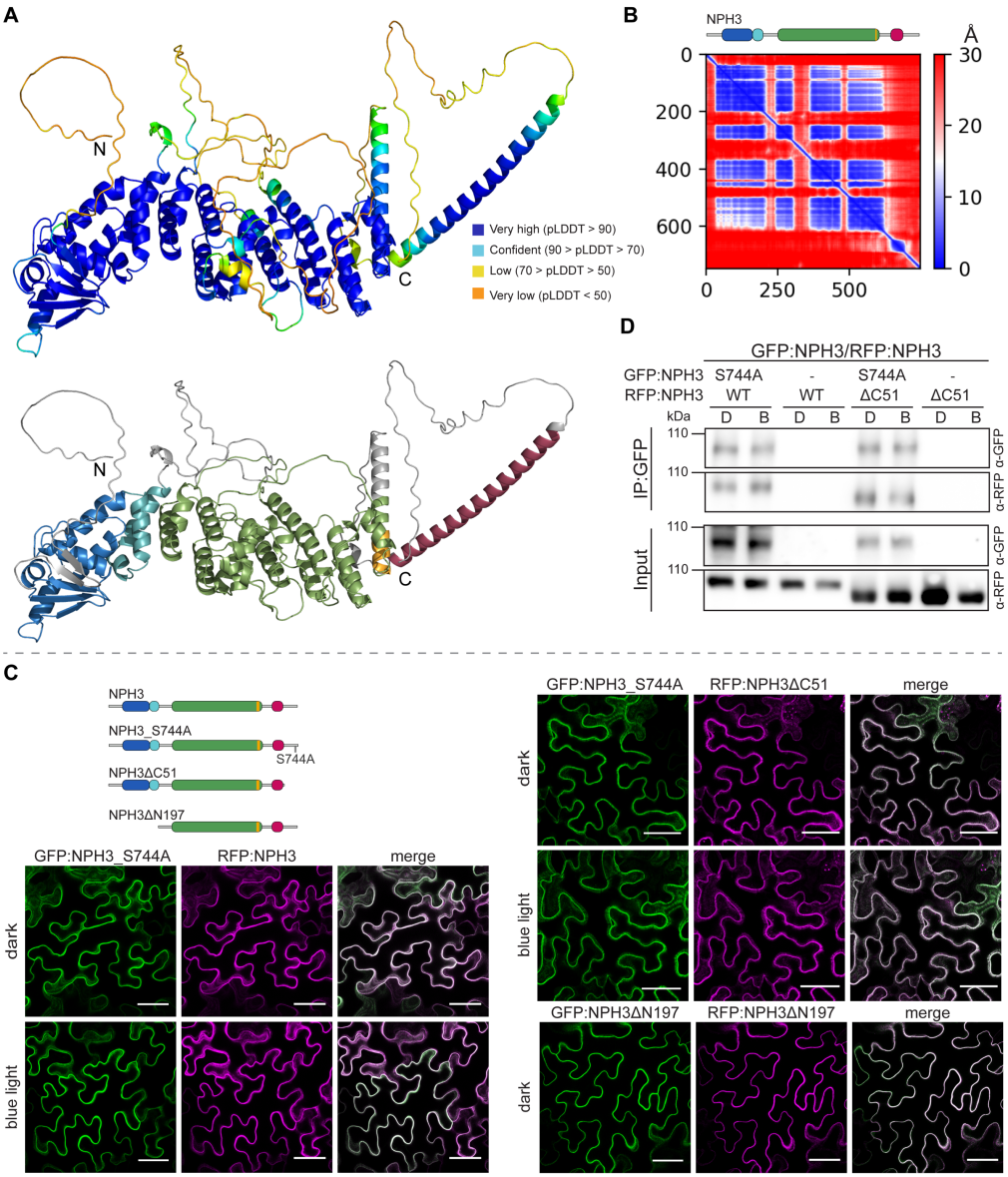

Figure EV1. Self-association of NPH3 is independent of its subcellular localization.
(**A**) Protein structure of NPH3 predicted by AF2. Color-coding of the ribbon plot is based either on the 'per residue confidence score' (pLDDT, **upper panel**) or on the schematic domain representation (Fig. 1A) (**lower panel**). N, N-terminus; C, C-terminus. (**B**) PAE plot of the NPH3 structure shown in (A). (**C**) Representative confocal images of leaf epidermal cells from *N. benthamiana* transiently co-expressing (35S promoter) GFP/RFP:NPH3 variants. Dark-adapted tobacco plants were either kept in darkness or treated with BL (~ 11 min GFP laser). Z-stack projections are shown, except for GFP:NPH3ΔN197/RFP:NPH3ΔN197. Scale bars, 50 µm. These experiments were repeated at least three times with similar results. (**D**) *In vivo* interaction of GFP/RFP:NPH3 variants transiently co-expressed (35S promoter) in *N. benthamiana* leaves. Dark-adapted tobacco plants were either kept in darkness (D) or treated with BL (B) (10 µmol $m^{-2}s^{-1}$, 1h). The crude protein extract was immunoprecipitated using GFP beads. Immunodetection of input and immunoprecipitated proteins (IP:GFP) is shown. Experiments were performed at least two times with similar results.

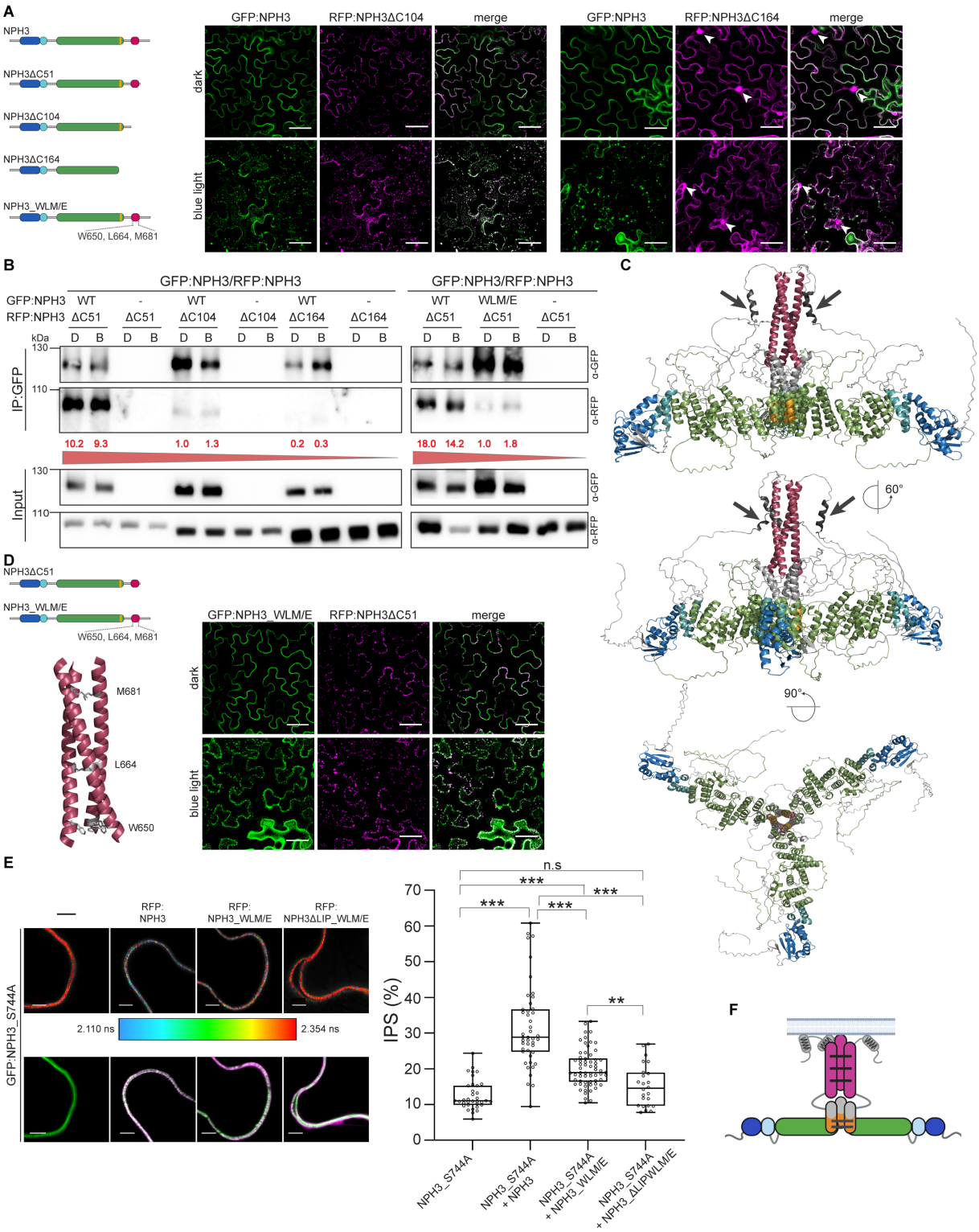

Figure 2. NPH3 is characterized by a bipartite C-terminal self-association motif.
(**A**, **D**) Schematic representation of NPH3 variants used and representative confocal images of leaf epidermal cells from *N. benthamiana* transiently co-expressing (35S promoter) different GFP/RFP:NPH3 variants. Dark-adapted tobacco plants were either kept in darkness or treated with BL (~ 11 min GFP laser). Z-stack projections of BL-treated samples are shown. Scale bars, 50 µm. Experiments were repeated at least three times with similar results. White arrowheads indicate nucleus. (**B**) *In vivo* interaction of GFP/RFP:NPH3 variants transiently co-expressed (35S promoter) in *N. benthamiana* leaves. Dark-adapted tobacco plants were either kept in darkness (D) or treated with BL (B) (10 µmol $m^{-2}s^{-1}$, 1h). The crude protein extract was immunoprecipitated using GFP beads. Immunodetection of input and immunoprecipitated proteins (IP:GFP) is shown. Experiments were performed at least two times with similar results. Values in red: normalized RFP/GFP intensity ratio. (**C**) Ribbon plot of the NPH3 trimer predicted by AF2M and color-coded according to the schematic domain representation (Fig. 1A). Grey arrow: amphipathic helix. (**E**) Interaction Pixels Analysis based on FRET-FLIM measurements

performed on leaf epidermal cells from dark-adapted *N. benthamiana* transiently (co-)expressing (35S promoter) GFP:NPH3_S744A and RFP-tagged NPH3 variants. Representative color-coded FLT images (2.354 ns: mean FLT of donor-only, 2.110 ns: IPS threshold) (**upper panel**) and merged confocal images (**lower panel**) are shown. Scale bars, 5 µm. Statistical differences in IPS were analyzed using Kruskal-Wallis test, followed by a Dunn post hoc analysis with Holm-adjusted p-values (** $p < 0.01$, *** $p < 0.001$, n.s. non significant) (**right panel**). Center line: median, bound of boxes: minima and maxima (25th and the 75th percentiles), whiskers: 1.5 x IQR. Number of cells analyzed (from left to right): 35, 45, 63, 24. (**F**) Schematic model of NPH3 illustrating the self-association of NPH3 at the PM mediated by the bipartite C-terminal motif. Color-coding according to the schematic domain representation (Fig. 1A). Dark and light grey bars indicate high and low affinity, respectively.

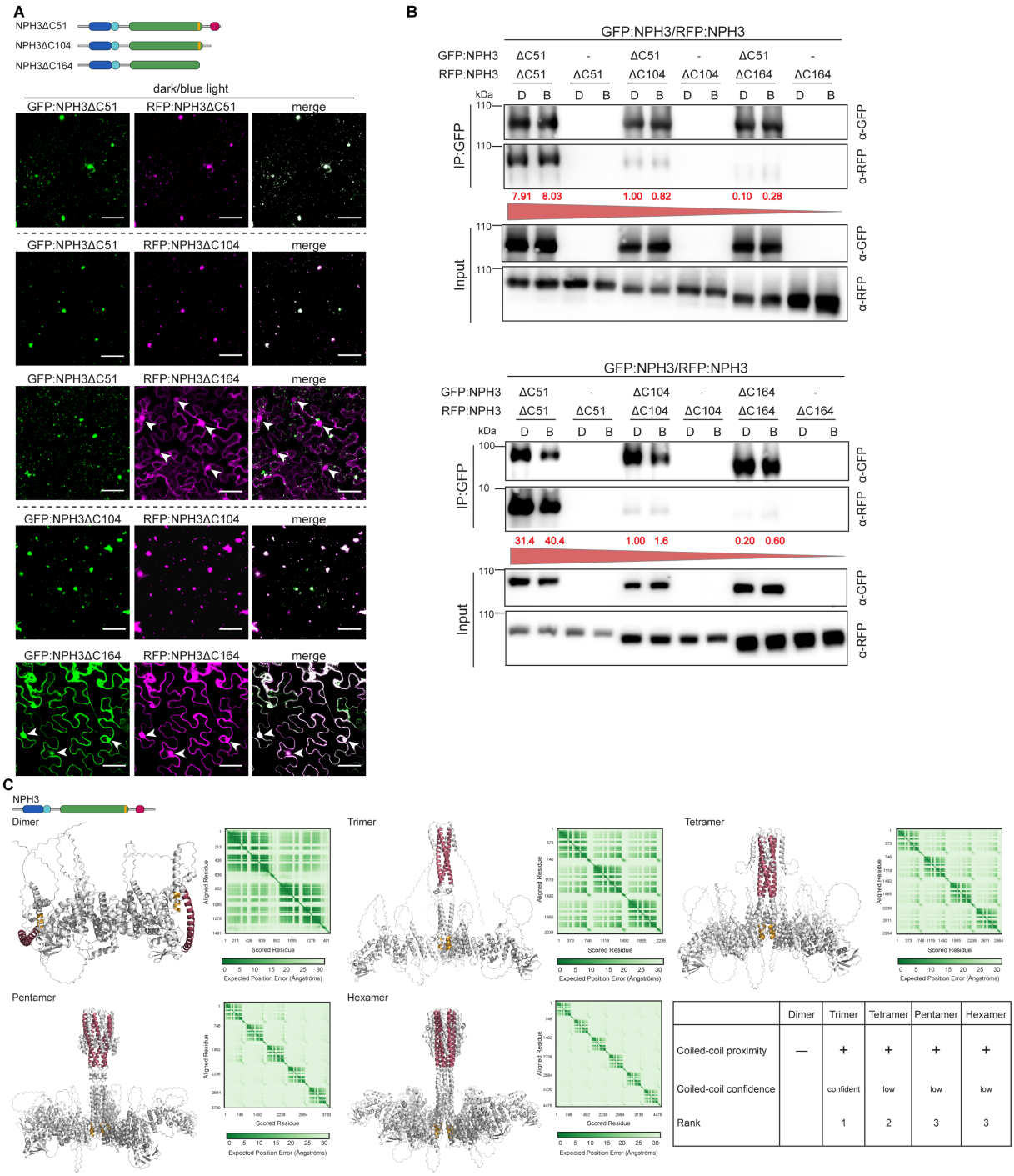

	Dimer	Trimer	Tetramer	Pentamer	Hexamer
Coiled-coil proximity	—	+	+	+	+
Coiled-coil confidence		confident	low	low	low
Rank		1	2	3	3

Figure EV2. The bipartite C-terminal self-association motif of NPH3 consists of the CC domain and the LIP motif.

(**A**) Schematic representation of NPH3 variants used and representative confocal images of leaf epidermal cells from *N. benthamiana* transiently co-expressing (35S promoter) GFP/RFP:NPH3 variants. Dark-adapted tobacco plants were either kept in darkness or treated with BL (~ 11 min GFP laser). Z-stack projections are shown. Scale bars, 50 µm. Experiments were performed at least three times with similar results. White arrowheads indicate nucleus. (**B**) *In vivo* interaction of GFP/RFP:NPH3 variants transiently co-expressed (35S promoter) in *N. benthamiana* leaves. Dark-adapted tobacco plants were either kept in darkness (D) or treated with BL (B) (10 µmol $m^{-2}s^{-1}$, 1h). The crude protein extract was immunoprecipitated using GFP beads. Immunodetection of input and immunoprecipitated proteins (IP:GFP) is shown. Experiments were performed at least three times with similar results. Values in red: normalized RFP/GFP intensity ratio. (**C**) Ribbon plot and PAE plot of NPH3 homooligomers predicted by AF3. The CC domain and the LIP motif are color-coded according to the schematic domain representation (Fig. 1A). A comparative analysis of the characteristics of the respective homooligomers is given.

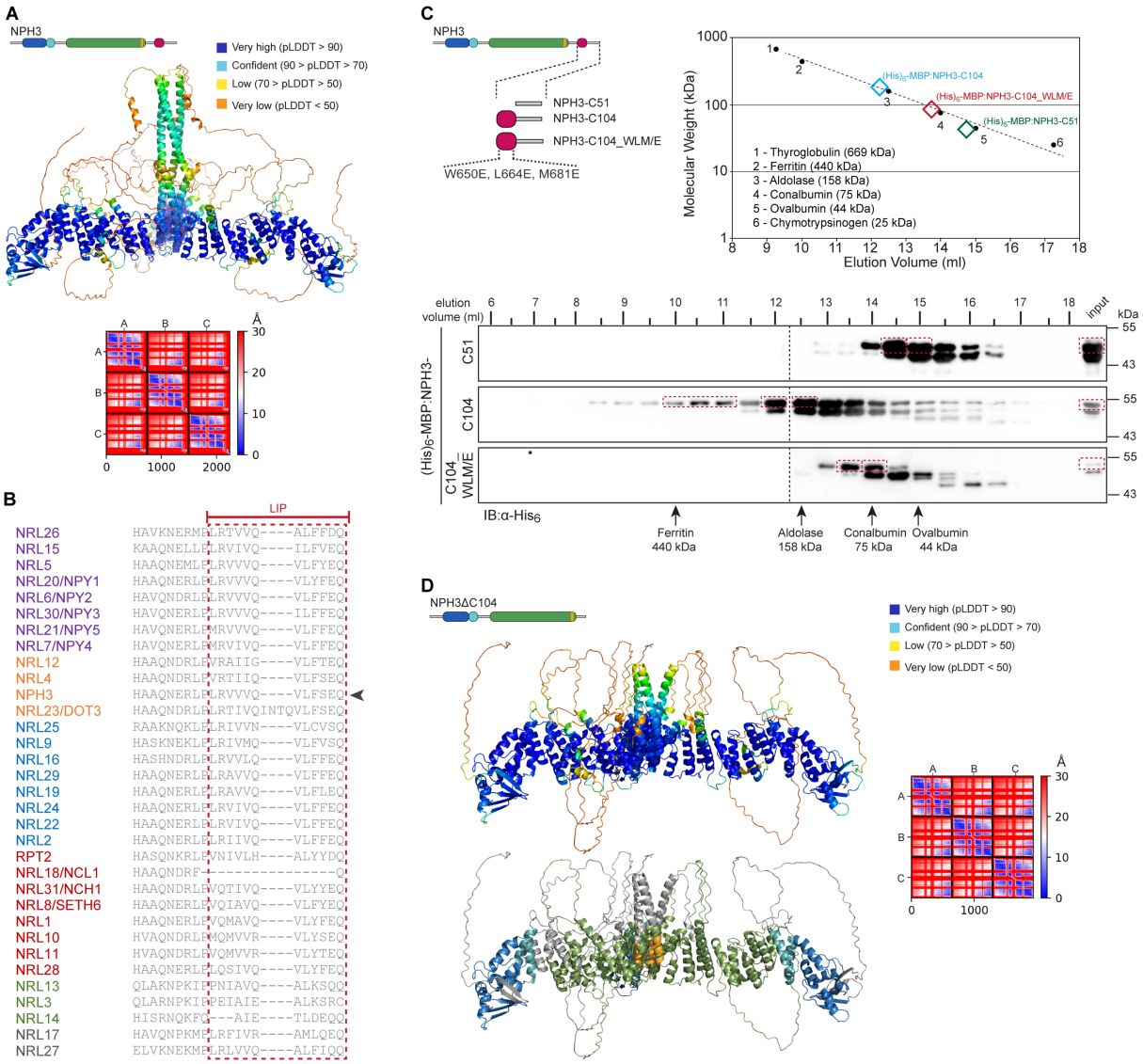

Figure EV3. Homo-oligomerization of the CC domain and LIP motif conservation.
(**A**) Ribbon plot of NPH3 trimer predicted by AF2M and color-coded according to the pLDDT score (**upper panel).** The corresponding PAE plot is shown in the **lower panel**. (**B**) Amino acid alignment of the *Arabidopsis* NRL protein family focusing on the residues constituting the LIP motif in NPH3 (red dotted box). (**C**) Schematic representation of C-terminal NPH3 fragments **(left panel)** and size exclusion chromatography **(right panel)** of the purified fragments tagged with $(His)_6$-Maltose Binding Protein (MBP). Elution of molecular mass marker proteins (1-6) is indicated within the graph. Molecular weights of the proteins are given in logarithmic scale (Y-axis). The α-His immunological analysis of fractions obtained via size exclusion chromatography is shown in the **lower panel**. The red dotted boxes highlight the purified non-degraded fusion protein in the input as well as in the elution fractions. Arrows mark the elution peaks of the marker proteins with the indicated molecular mass. (**D**) Ribbon plot of the NPH3ΔC104 trimer predicted by AF2M and color-coded according to the pLDDT score (**upper left panel**) or the schematic domain representation (Fig. 1A) (**lower left panel).** The corresponding PAE plot is shown in the **right panel**.

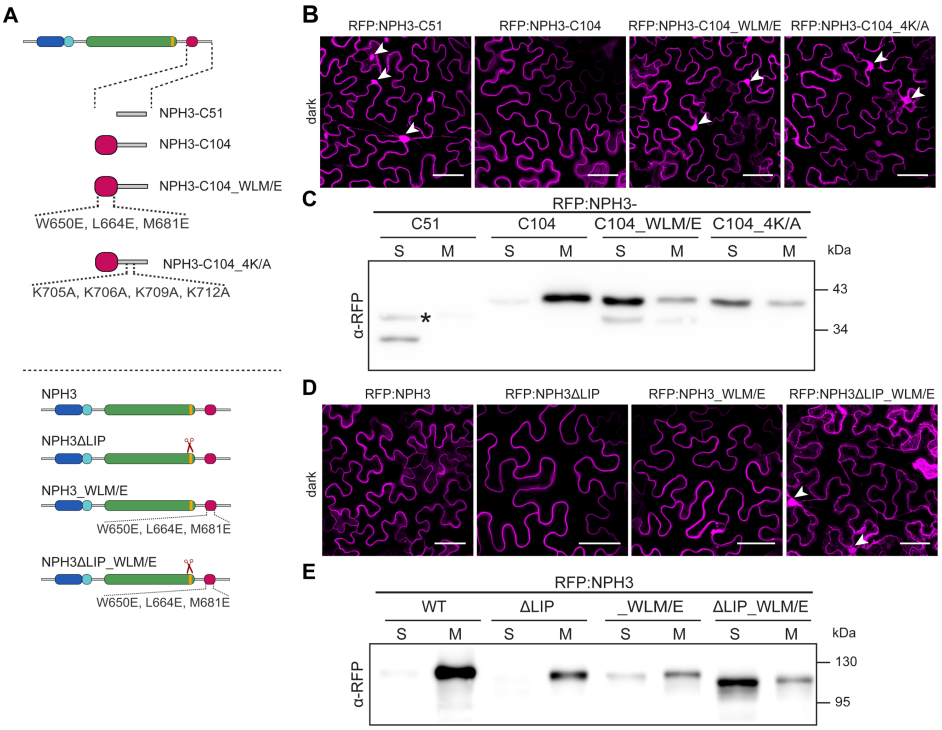

Figure 3. Homo-oligomerization mediated by the bipartite motif is essential for PM association of NPH3 *in vivo*.

(**A**) Schematic representation of C-terminal NPH3 fragments and NPH3 variants used. (**B, D**) Representative confocal images of leaf epidermal cells from dark-adapted *N. benthamiana* transiently expressing (35S promoter) RFP:NPH3 variants. Z-stack projections are shown. Scale bars, 50 µm. White arrowheads indicate nucleus. (**C, E**) Representative α-RFP immunoblots following subcellular fractionation of protein extracts prepared from dark-adapted *N. benthamiana* leaves transiently expressing (35S promoter) RFP:NPH3 variants. Proteins in each fraction (~ 10 µg) were separated on SDS-PAGE gels. It is noteworthy that the total amount of soluble proteins (S) is ~10 times higher as compared to the total amount of microsomal proteins (M). (*) Asterisk indicates non-specific band. All experiments were performed at least three times with comparable results.

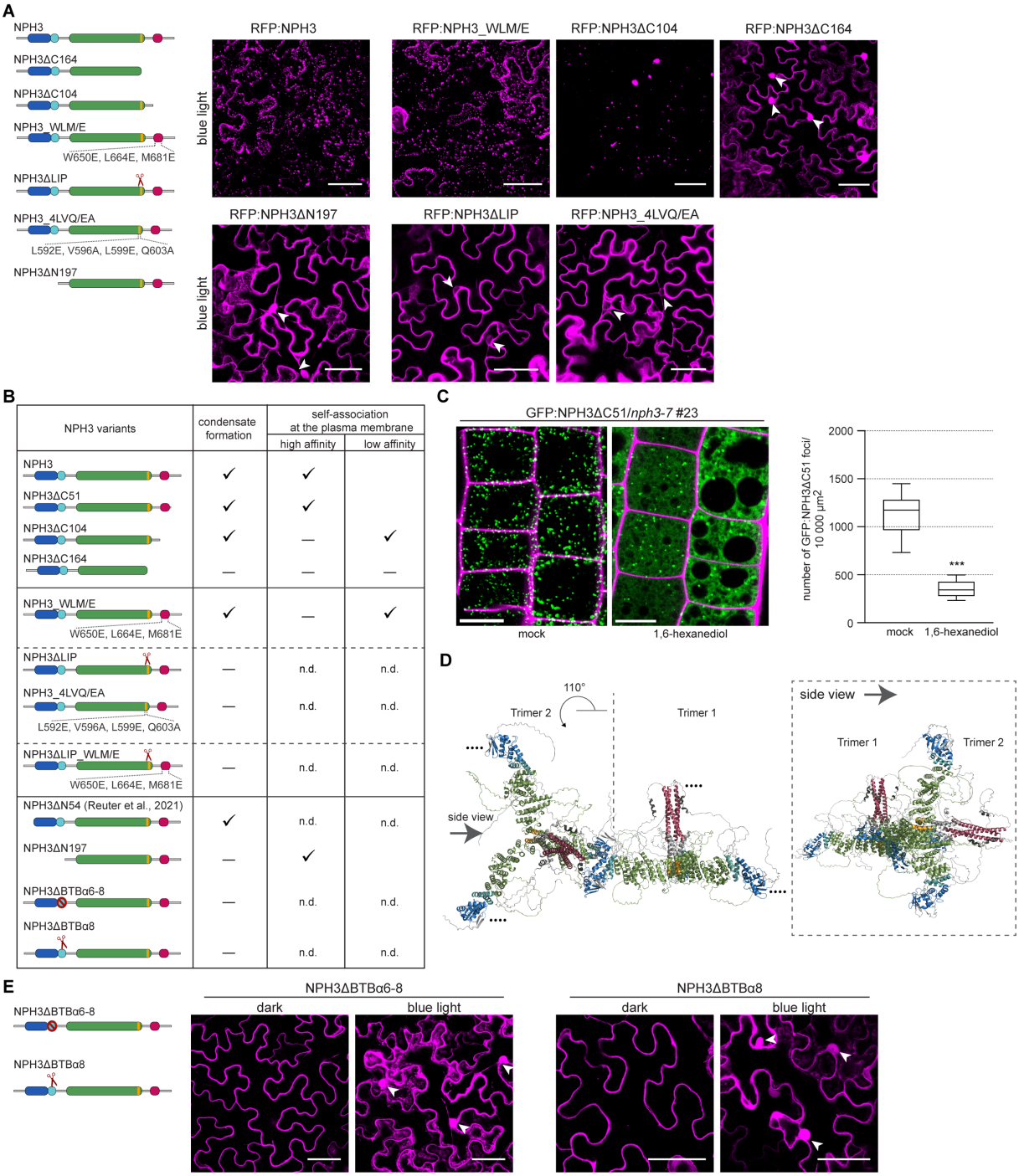

Fig. 4. Condensate assembly of NPH3 requires the LIP motif and the BTB domain.
(**A**, **E**) Schematic representation of NPH3 variants used (LIP motif highlighted in yellow, see text for details) and representative confocal images of leaf epidermal cells from *N. benthamiana* transiently expressing (35S promoter) RFP:NPH3 variants. Dark-adapted tobacco plants were treated with BL (~ 11 min GFP laser). Z-stack projections of BL-treated samples are shown. Scale bars, 50 µm. White arrowheads indicate nucleus/cytoplasmic strands. All experiments were repeated at least three times with similar results. (**B**) Summary of NPH3 variants and their ability to self-associate at the plasma membrane and form cytosolic condensates. n.d. not determined. (**C**) Representative confocal images of root epidermal cells from 4-day-old light grown *Arabidopsis nph3-7* seedlings ectopically expressing constitutively condensate-forming GFP:NPH3ΔC51 and treated with 1,6-hexanediol or mock in the presence of propidium iodide (**left panel**). Note the increase in cytoplasmic GFP:NPH3ΔC51 levels upon hexanediol treatment. Scale bars: 10 µm. The **right panel** shows the number of condensates. n = 24 seedlings (untreated), n = 24 seedlings (1,6-hexanediol); untreated/1,6-hexandiol P = <0.0001 (***P < 0.001). (**D**) Ribbon plot of two NPH3 trimers crosslinked via antiparallel BTB-BTB interaction, resulting in a rotation of the second trimer by approx. 110°. Note that each trimer comprises two additional BTB domains that could be crosslinked. The corresponding side view (arrow) highlights the different orientation of the trimers.

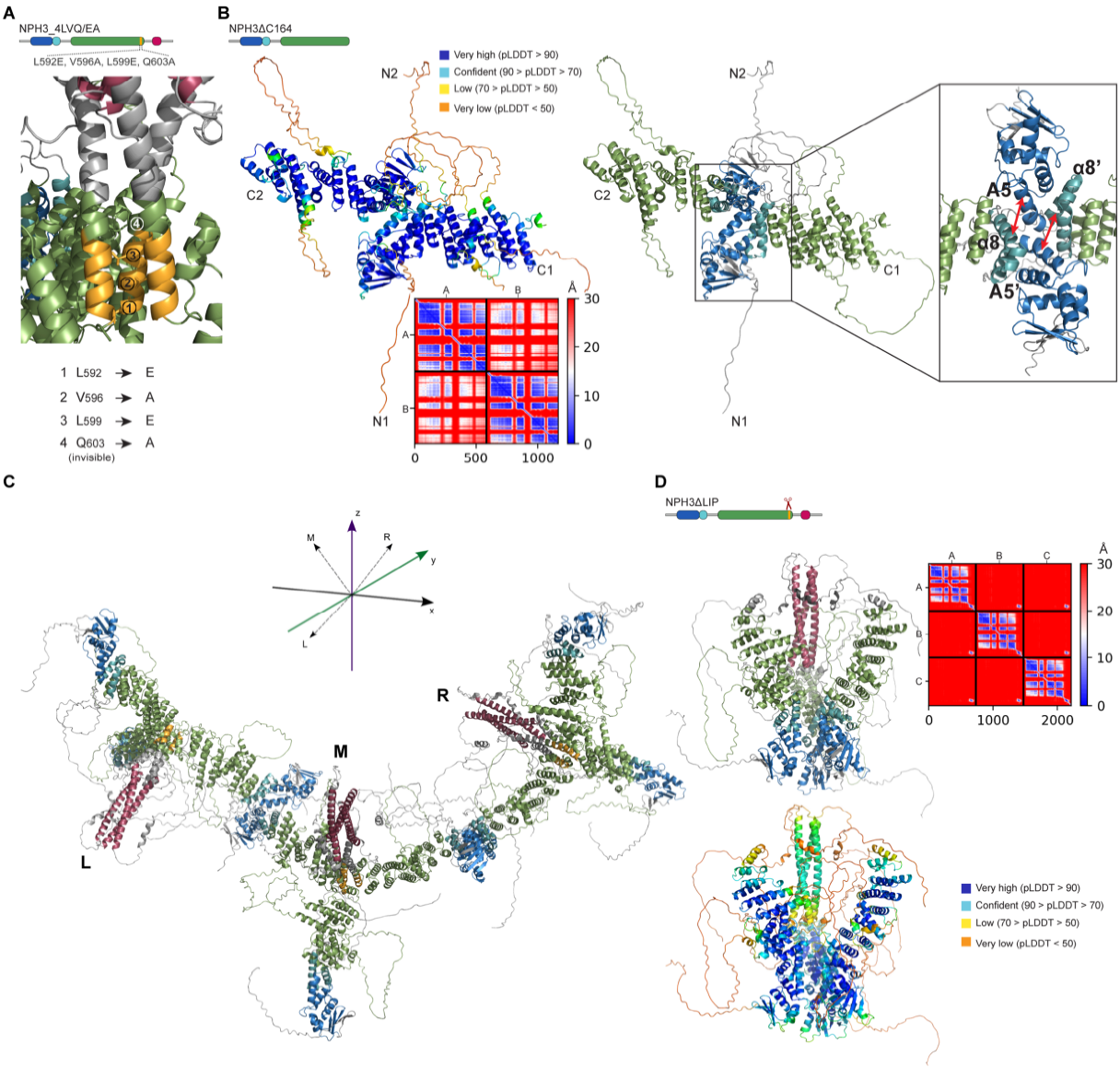

Figure EV4. Crosslinking of NPH3 trimers via BTB-dependent antiparallel interactions could enable the formation of higher-order assemblies.

(**A**) Enlarged view of the LIP helix bundle showing the position of the mutated residues. (**B**) Ribbon plot of the NPH3ΔC164 dimer predicted by AF2M and color-coded according to the pLDDT score (**left panel**) or the schematic domain representation (Fig. 1A) (**right panel**) or the pLDDT score. The corresponding PAE plot is shown in the **lower panel**. Enlarged view depicts the potential antiparallel BTB-BTB interaction based on the interaction between helix A5 of the core BTB (dark blue) and helix α8 of the C-terminal BTB extension (light blue). N1, N2, N-terminus; C1, C2, C-terminus. (**C**) Ribbon plot of three NPH3 trimers crosslinked via antiparallel BTB-BTB interaction. Note that each trimer comprises one or two additional BTB domains that could be crosslinked. The pictogram indicates the position of each CC domain in 3D space. (**D**) Ribbon plot of the NPH3ΔLIP trimer predicted by AF2M and color-coded according to the schematic domain representation (**upper panel left**) or the pLDDT score **(lower panel**). The corresponding PAE plot is shown in the **upper right panel**.

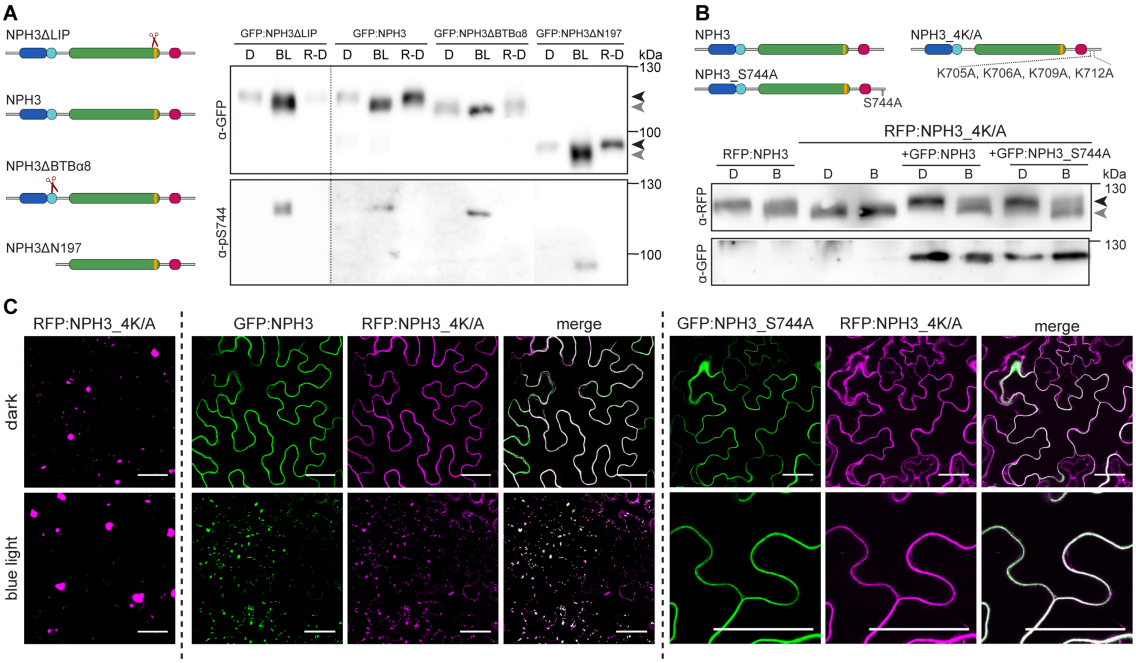

Fig. 5. Phot1-dependent dephosphorylation of NPH3 is independent of condensate formation and PM dissociation.

Black and grey arrowheads indicate the position of the phosphorylated and dephosphorylated NPH3 proteins, respectively. (**A**, **B**) Schematic representation of NPH3 variants used and immunoblot analysis of total protein extracts from *N. benthamiana* leaves transiently (co-)expressing (35S promoter) GFP/RFP:NPH3 variants. Dark-adapted tobacco plants were either maintained in darkness (D), treated with BL (10 µmol $m^{-2}s^{-1}$, 1h) (BL) or re-transferred to darkness (30 min) after irradiation (R-D). Proteins were separated on a 7.5 % SDS-PAGE gel. The dotted line indicates that NPH3ΔLIP (as compared to NPH3) was analyzed on a different gel.
(**C**) Representative confocal images of leaf epidermal cells from *N. benthamiana* transiently co-expressing (35S promoter) RFP:NPH3_4K/A either with GFP:NPH3 or GFP:NPH3_S744A. Dark-adapted tobacco plants were either kept in darkness or treated with BL (~ 11 min GFP laser). Single expression of RFP:NPH3_4K/A is shown as control. Z-stack projections of the single expression of RFP:NPH3_4K/A and of BL-treated samples are shown. Scale bars, 50 µm. All experiments were repeated at least three times with similar results.

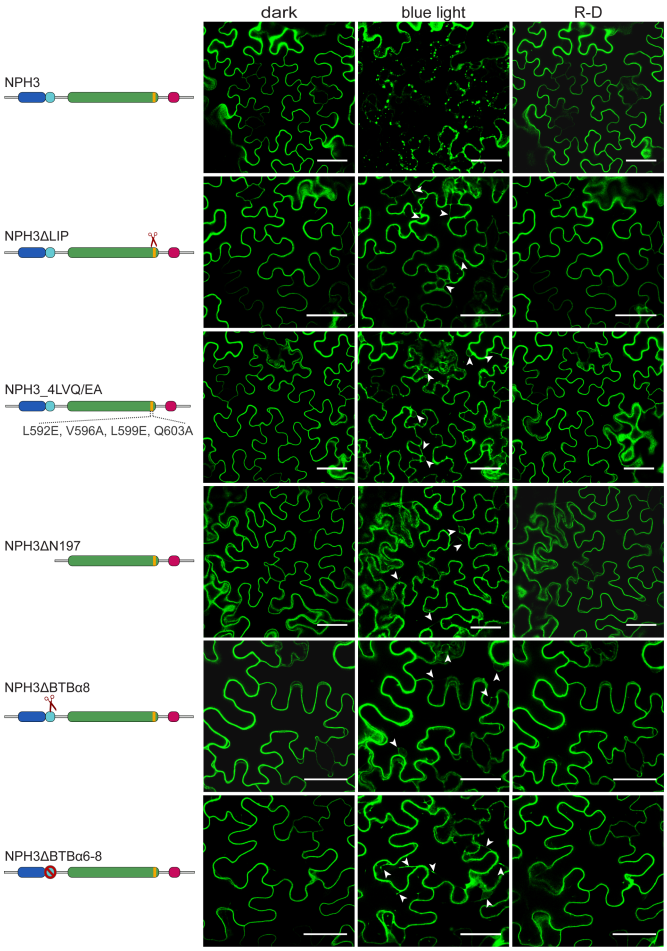

Figure EV5. Light-dependent changes in subcellular localization are retained in condensate-incompetent NPH3 variants.

Schematic representation of NPH3 variants used and representative confocal images of leaf epidermal cells from *N. benthamiana* transiently expressing (35S promoter) different GFP:NPH3 variants. Dark-adapted tobacco plants were either maintained in darkness (dark), treated with BL (~ 11 min GFP laser) or re-transferred back to darkness (30 min) after irradiation (R-D). Scale bars, 50 µm. Experiments were repeated at least three times with similar results. White arrowheads indicate cytoplasmic strands.

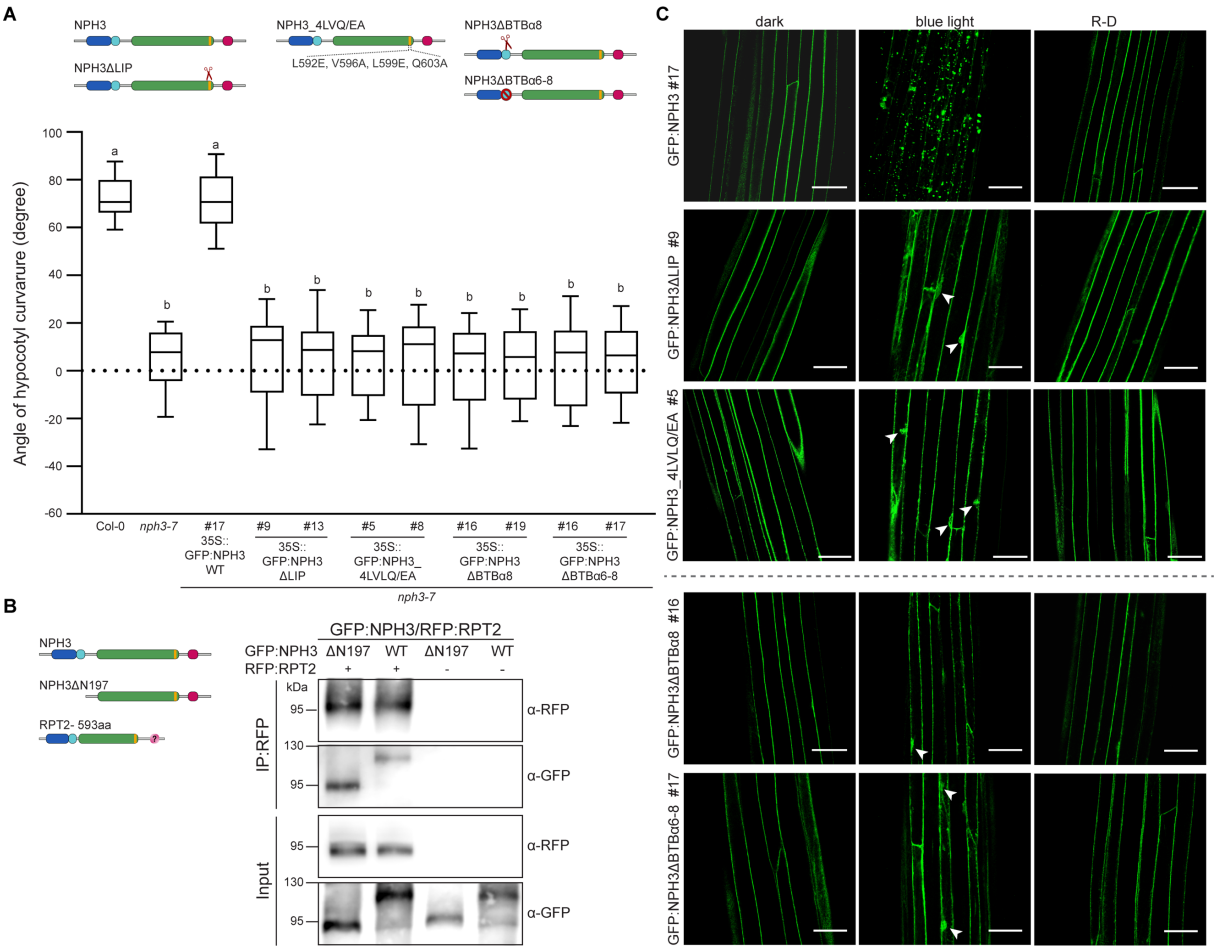

Fig. 6. Functional relevance of NPH3 condensate formation.
(**A**) Quantification of hypocotyl phototropism (mean ± SD) in etiolated *Arabidopsis nph3-7* seedlings ectopically expressing GFP:NPH3 variants and exposed to unilateral BL (0.1 µmol m^{-2} s^{-1}, 24 h) ($n \geq 30$ seedlings per experiment, three replicates). One way ANOVA with Tukey's post-hoc test is shown, different letters mark statistically significant differences ($p < 0.05$). Centre line: median, bounds of box: minima and maxima (25th and 75th percentiles), whiskers: 1.5 × IQR. Exact p-values for all experiments are provided in the source data file. (**B**) *In vivo* interaction of GFP:NPH3 variants transiently co-expressed (35S promoter) with RFP:RPT2 in *N. benthamiana* leaves (dark-adapted). The crude protein extract was immunoprecipitated using RFP beads. Immunodetection of input and immunoprecipitated (IP:RFP) proteins is shown. Experiments were performed at least two times with similar results. (**C**) Representative confocal microscopy images of hypocotyl cells from 3-day-old etiolated *Arabidopsis* seedlings shown in (A)**,** and either maintained in darkness (dark), treated with BL (1 µmol $m^{-2}s^{-1}$) for 1 hour or re-transferred to darkness (1 h) after irradiation (R-D). Note that when analyzing the three transgenic lines shown below the dashed line, GFP laser power was increased due to a weaker expression of the transgenes (Fig. EV6). Z-stack projections of BL- treated samples are shown. Scale bars, 50 µm. Experiments were performed at least two times with similar results. Arrowheads indicate nucleus.

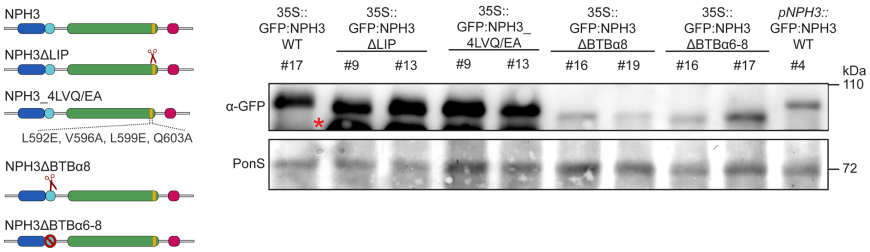

Figure EV6. Expression level of NPH3 variants in transgenic Arabidopsis lines.
Schematic representation of NPH3 variants used and immunoblot analysis of total protein extracts from 3-day-old etiolated Arabidopsis *nph3-7* seedlings expressing (35S promoter) GFP-tagged NPH3 variants. Proteins (approx. 15 µg) were separated on 8 % SDS-PAGE gels and subsequently immunodetected with an anti-GFP antibody. Red asterisk indicates degradation product. Immunodetection of native promoter driven NPH3 expression, which restores the phototropic response of *nph3-7* (Reuter *et al*, 2021; Sullivan *et al*, 2021), is shown for comparison. PonS - Ponceau Staining.

Table EV1. Blue-light dependent NPH3 interactors in etiolated Arabidopsis seedlings.
Analysis of GFP:NPH3 immunoprecipitates via mass spectrometry based on two biological replicates. This table lists only NPH3 clients showing at least a twofold increase in normalized iBAQ values following BL irradiation. Protein intensities were converted to the relative abundance (%) of the bait protein and client proteins showing a value ≥ 1 % are highlighted in light red.

1092

Mutagenesis primers	
NPH3_L_{592}E/V_{596}A_F	AACGAGAGGTTGCCAgaGAGAGTGGTGGcTCAAGTTCTCTTCTC
NPH3_L_{592}E/V_{596}A_R	GAGAAGAGAACTTGAgCCACCACTCTCtcTGGCAACCTCTCGTT
NPH3_V_{596}A/L_{599}E/Q_{603}A_F	GTGGTGGcTCAAGTTgaaTTCTCGGAGgcAGTCAAGATCAGCAA
NPH3_V_{596}A/L_{599}E/Q_{603}A_R	TTGCTGATCTTGACTgcCTCCGAGAAttcAACTTGAgCCACCAC
NPH3_L_{664}E _F	AACACGTTGAAGTTCGAGgaAGAGACGGTGAAGACCAAG
NPH3_ L_{664}E _R	CTTGGTCTTCACCGTCTCTtcCTCGAACTTCAACGTGTT
NPH3_M_{681}E_F	CAGAACGAGATGGAAGTGgaGCAACGACAGTTTGAGAAG
NPH3_M_{681}E_R	CTTCTCAAACTGTCGTTGCtcCACTTCCATCTCGTTCTG
NPH3_W_{650}E_F	CAATCGTTTCAGGAAGGAgaGGCTGCAGCCAAGAAGGAT
NPH3_W_{650}E_R	ATCCTTCTTGGCTGCAGCCtcTCCTTCCTGAAACGATTG
Primer extension PCR (deletion constructs)	
NPH3ΔLIP_F	CAGAACGAGAGGTTGCCATCGGAGCAAGTCAAGATC
NPH3ΔLIP_R	GATCTTGACTTGCTCCGATGGCAACCTCTCGTTCTG
NPH3ΔBTBα6-8_F	GTGGTTCTGTCTTCATGGAGTAATCCAAAAGGTATT
NPH3ΔBTBα6-8_R	AATACCTTTTGGATTACTCCATGAAGACAGAACCAC
NPH3ΔBTBα8_F	TGTGAAAAGCTCTCACCTAGTAATCCAAAAGGTATT
NPH3ΔBTBα8_R	AATACCTTTTGGATTACTAGGTGAGAGCTTTTCACA
GATEWAY	
NPH3_attB1_F	AAAAAGCAGGCTTAATGTGGGAATCTGAGAGCGAC
NPH3_attB2_R	AGAAAGCTGGGTGTCATGAAATTGAGTTCCTCCA
NPH3_S744A_attB2_R	Reuter *et al*, 2021
NPH3ΔN197_attB1_F	AAAAAGCAGGCTTAATGAGTAATCCAAAAGGTATTAGA
NPH3ΔC51_attB2_R	Reuter *et al*, 2021
NPH3ΔC104_attB2_R	AGAAAGCTGGGTGTCATGTTGCTTCGATCAATGTCTT
NPH3ΔC164_attB2_R	AGAAAGCTGGGTGTCACATACATGCGTCCATTGATAG
NPH3-C104_attB1_F	AAAAAGCAGGCTTAATGCCACAATCGTTTCAGGAAGGA
RPT2_attB1_F	AAAAAGCAGGCTTAATGGCAACAGAAGGAAAAAACCCCA
RPT2_attB2_R	AGAAAGCTGGGTGTTAAGAGATTGAGAATCTTCGTCTC
TOPO cloning	
NPH3-C51_F	CACCATGTCTTCTTCGGCTTGGACCAG

1093

1094 **Table EV2. List of primers used in this study.**